PSFC/RR-99-12 DOE/ET-54512-334

Transport of Particles and Energy in the Edge Plasma of the Alcator C-Mod Tokamak

M. Umansky

Plasma Science and Fusion Center
Massachusetts Institute of Technology
Cambridge, MA 02139

September 1999

This work was supported by the U. S. Department of Energy Contract No. DE-FC002-99ER54512. Reproduction, translation, publication, use and disposal, in whole or in part by or for the United States government is permitted.

Transport of particles and energy in the edge plasma of the Alcator C-Mod tokamak

by

Maxim Umansky

M.Sc. (Hons.), Plasma Physics and Chemistry (1993)
Moscow Institute of Physics and Technology

Submitted to the Department of Physics
in partial fulfillment of the requirements for the degree of

Doctor of Philosophy in Physics

at the

MASSACHUSETTS INSTITUTE OF TECHNOLOGY

February 2000

Author .....
Department of Physics
October 5, 1999

Certified by .....
Earl S. Marmar
Senior Research Scientist
Thesis Supervisor

Accepted by .....
Thomas J. Greytak
Professor, Associate Department Head for Education

Transport of particles and energy in the edge plasma of the Alcator C-Mod tokamak

by

Maxim Umansky

Submitted to the Department of Physics
on October 5, 1999, in partial fulfillment of the
requirements for the degree of
Doctor of Philosophy in Physics

Abstract

In this thesis analysis and numerical modeling of transport in the edge plasma in the Alcator C-Mod tokamak are presented. Several important results were obtained in the course of this work, providing a new understanding of some aspects of the physical picture of the edge plasma in C-Mod. The key finding are:

- Plasma escaping from the core recycles on the main chamber wall rather than in the divertor. Thus plasma recycling occurs largely independently in the main chamber and in the divertor chamber.
- The radial particle transport in the scrape-off layer (SOL) is radially non-uniform with the "effective" anomalous diffusion coefficient $D_\perp$ growing by more than an order of magnitude across the SOL.
- Heat flux carried out of the core plasma across the last closed flux surface is in most cases dominated by radial convection and charge-exchange (CX) neutrals rather than by anomalous heat diffusion. In certain regimes convection and CX heat conduction dominate the radial heat transport across the whole SOL.
- The main chamber neutral gas density reflects the level of anomalous particle transport from the core plasma rather than the quality of neutral gas baffling in the divertor.
- The core plasma is fueled by neutrals diffusing into the core mainly through the lower half of the last closed flux surface.

As these findings touch on the most basic issues in the tokamak edge physics, these results contribute to our understanding of the tokamak edge plasmas in general, although they may not fully apply to other tokamaks.

Thesis Supervisor: Earl S. Marmar
Title: Senior Research Scientist

Acknowledgments

I would like to acknowledge the support and guidance of my dissertation advisors, Dr. Brian LaBombard and Prof. Sergei Krasheninnikov. Working with such a remarkable theorist as Sergei contributed greatly to the breadth of my plasma physics thinking while Brian shared with me his incredible experience and intuition in experimental plasma physics.
I would like to thank my thesis readers Dr. Earl Marmar, Prof. Miklos Porkolab and Prof. Vicky Kaspi for many insightful suggestions and comments.
This thesis would not be possible if not for the work of the scientists, engineers, technicians, and graduate students of the C-Mod group and I would like to thank them all.
But most of all I would like to acknowledge the love and support of my wife Anna and our daughter Vera.

Contents

List of Figures

List of Tables

Chapter 1

Introduction

1.1 Thermonuclear fusion

Atomic nuclei can undergo nuclear reactions producing other nuclei and elementary particles. One category of such reactions, fission, is a decay process where an unstable nucleus breaks into two or more fragments, the sum of whose binding energies is greater than that of the original nucleus. Conversely in a fusion reaction two nuclei form a heavier nucleus. Generally energy is released in fusion of light nuclei ($A \lesssim 50$) and in fragmentation of a heavy nucleus ($A \gtrsim 50$) since the potential energy of the system is lowered in such processes. Most stable nuclei with minimal potential energy (per nucleon) have atomic mass close to $A \sim 50$.

Fusion of light nuclei is a widespread natural phenomenon providing the source of energy in stars. Generally a self-sustaining fusion reaction requires high temperature (10^7 K and more) which is a significant obstacle to achieving such a reaction artificially. Thus one of the most important considerations for artificial thermonuclear fusion is the ignition temperature i.e. the temperature which must be achieved before the fusion reaction can become self-sustaining. Due to the Coulomb barrier the general trend is that the ignition temperature is lower for lighter nuclei. This is why

fusion of lightest nuclei i.e. isotopes of hydrogen is the most attractive for an artificial fusion reaction.

For the fusion reaction to occur the reacting nuclei must be brought to each other close enough to let the internuclear attraction force bind them together. In the classical theory this implies that the nuclei must have kinetic energy above the Coulomb barrier

$$E_c = Z_1 Z_2 \frac{e^2}{R_0} \tag{1.1}$$

where the Z_1, Z_2 are the atomic numbers of two reacting nuclei and R_0 is the distance at which the nuclear attraction becomes dominant. For hydrogen isotopes Z=1 and for light nuclei R_0 can be taken as approximately equal to the nuclear diameter, $R_0 \sim 5 \times 10^{-13}$ cm which gives $E_c \sim 0.28$ MeV. However the quantum tunneling effect causes the fusion reaction to have a non-zero rate even for relative energy being smaller than the Coulomb barrier. Still in practice fusion requires very high temperature at which all atoms are completely ionized which corresponds to the plasma state of matter.

1.1.1 Fusion of hydrogen isotopes

An obstacle to the fusion of hydrogen H into heavier nuclei is that all stable nuclei heavier than hydrogen must contain neutrons. This is why burning of hydrogen which naturally occurs in stars has to be a multi-stage process where in the first stage deuterium is formed in β decay process

$$H + H \rightarrow D + e^+ + \nu + 0.42MeV \tag{1.2}$$

and then a reaction between hydrogen and deuterium becomes possible. However intervention of a β decay makes this reaction intolerably slow for artificial fusion.

Other reactions involving H

$$H + D \rightarrow He^3 + \gamma \tag{1.3}$$

$$H + T \rightarrow He^4 + \gamma \tag{1.4}$$

are known to have cross-sections that are too small to permit a net gain of energy at an attainable temperature.

With deuterium D which reacts with itself there are several reactions possible

$$D + D \rightarrow \begin{cases} He^3 + n + 3.3MeV \\ T + H + 4.0MeV \\ He^4 + 23.8MeV \end{cases}$$

The last of these reactions has a negligible rate compared to the first two which have approximately equal rates.

Fusion of deuterium D and tritium T occurs according to

$$D + T \rightarrow He^4 + n + 17.6MeV \tag{1.5}$$

Another reaction of interest is

$$D + He^3 \rightarrow He^4 + H + 18.3MeV \tag{1.6}$$

In this reaction the products are charged particles only which has the potential for direct conversion of fusion energy into electricity.

The rates of main fusion reactions of interest as functions of temperature assuming Maxwellian distribution as tabulated in the NRL Plasma Formulary [1] are represented by graphs shown in Fig. 1.1. The D-T fusion rate is the highest for these

temperature as can be seen from Fig. 1.1. Thus for achieving ignition of fusion plasma it is easiest to use a 50-50 D-T mixture.

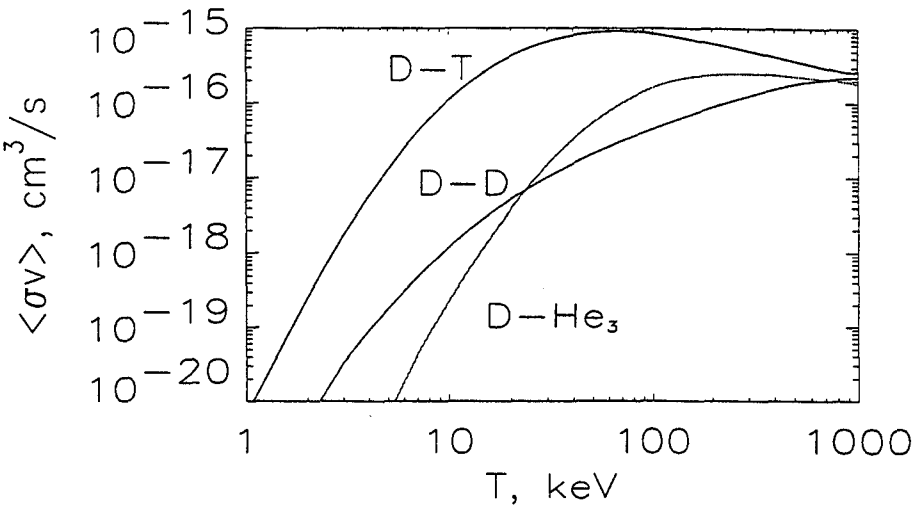

Figure 1.1: Fusion reaction rates

1.1.2 Lawson criterion

For ignition the produced fusion power should be greater than the energy losses from the plasma. If plasma is heated only by fusion power released in α-particles then for the case of D-T mixture the heating power per unit volume is

$$P_f = \frac{1}{4} n^2 < \sigma v > E_0 \tag{1.7}$$

where n is the ion density, $< \sigma v >$ is the D-T fusion rate averaged over Maxwellian distribution, $E_0 = 3.5$ MeV is the α-particle energy.

The energy losses rate is characterized by τ_E, the energy confinement time, and the

energy loss rate per per unit volume is

$$P_L = 3(nT)/\tau_E \tag{1.8}$$

Combining Eqs. 1.7 and 1.8 together one obtains the condition for self-sustaining burning

$$n\tau_E > \frac{12}{<\sigma v>}\frac{T}{E_0} \tag{1.9}$$

The right hand side of Eq. 1.9 has a minimum at $T \sim 30$ keV at which the ignition condition becomes [2]

$$n\tau_E > 1.5 \times 10^{14}\ (cm^{-3}s) \tag{1.10}$$

The latter is the Lawson criterion for burning plasma. A more detailed analysis [2] shows that for ignition temperature has to be about 10 keV.
The requirement for the temperature $T \sim 10$ keV and the Lawson criterion (Eq. 1.10) provide two main conditions for self-sustaining burning of a D-T plasma.

1.2 Advantages of fusion as an energy source

1.2.1 Inexhaustible energy source

The attractiveness of thermonuclear fusion as an energy source comes from a vast energy release in fusion reactions. The basic fusion material for fusion is deuterium which is present to the extent of 1 atom to 6500 atoms of ordinary hydrogen in water. In spite of this small proportion the amount of deuterium in one gallon of water could produce as much energy as burning of 300 gallons of gasoline. If all deuterium available in the oceans could be used for energy production the total energy release would be at least 10^{21} kilowatt-years. The world's present energy consumption rate is about 10^{10} kilowatts [2]. Thus the available deuterium would be sufficient for

practically unlimited time even with an increase by a large factor of earth's population and energy consumption per capita.

1.2.2 Environment-friendly energy source

Compared to the main present sources of energy such as the fossil fuels and the fission reactors the fusion reactor will be producing much less wastes per a unit of produced power. Production of CO_2 in burning of fossil fuels is believed to be possibly related to the greenhouse effect and global warming. In a fusion reaction no CO_2 will be produced. Unlike a fission reactor in a fusion reactor there will be no appreciable amount of radioactive material produced. However a fusion reactor will need a shielding from neutrons and other radiation.

1.2.3 Safety issues

In spite of the fact that a gram of deuterium is equivalent to the explosive energy of 80 tons of TNT, a fusion reactor can be expected to be completely safe. The reason is that at any time in a reactor there will be only a small amount of nuclear fuel which does not have enough energy to cause any damage. The thermonuclear fuel cannot explode by itself since the conditions for such self-sustaining reaction are extremely difficult to achieve.

1.3 Tokamak concept

1.3.1 Magnetic confinement

If plasma is in direct contact with a material wall it will rapidly lose its energy. By applying strong magnetic field one can provide insulation of plasma from the walls and thus achieve a large energy confinement time. In a magnetic field the

Lorentz force $F = v \times B$ makes charged particles gyrate about the magnetic field lines. However in the along-field direction the particle moves freely and an open-end magnetic configuration would suffer from end losses. To eliminate the open-end losses the magnetic configuration has to be closed; in a tokamak the configuration is toroidal. In addition, a helical twist is needed for the magnetic lines to establish a stable plasma configuration.

1.3.2 Tokamak design

In a tokamak the magnetic lines lie on nested toroidal magnetic flux surfaces (Fig. 1.2).

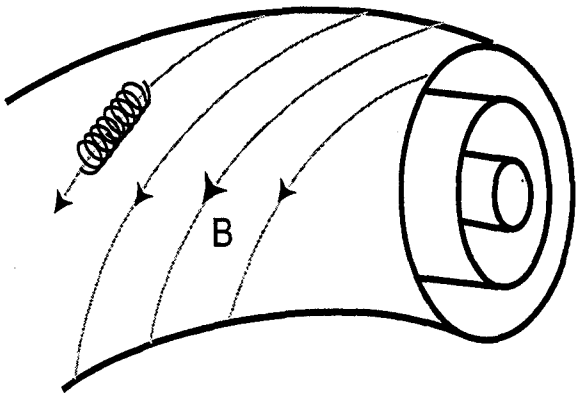

Figure 1.2: Magnetic flux surfaces in a tokamak. A charged particle is bound to the magnetic line and thus to the flux surface since in the cross-field direction its motion is constrained by the Lorentz force.

Here the helically-twisted magnetic field lines are obtained by superposition of a toroidal magnetic field created by external coils and a toroidal current flowing in plasma. The plasma current is also used for ohmic heating of the plasma. This current is induced by driving externally a time-dependent current in the winding around the tokamak core (see Fig. 1.3).

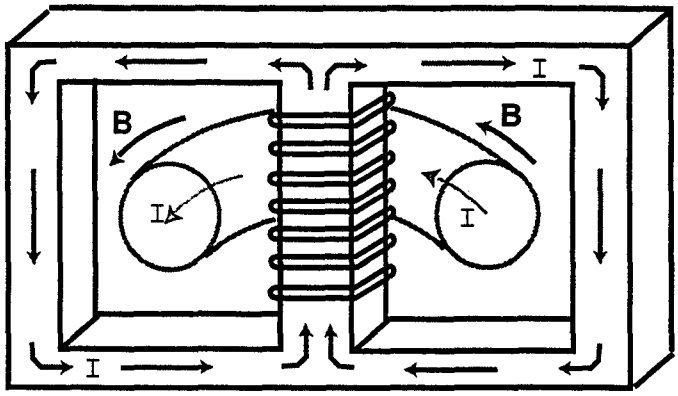

Figure 1.3: Schematic of a tokamak

1.3.3 Edge flux surfaces

For a closed flux surface a magnetic line can either close after a finite number of turns or wind infinitely. External flux surfaces which are in contact with the walls of the tokamak are not closed. Since it is desirable to minimize the contact between plasma and the walls one can use a so called limiter to keep plasma from touching the whole side wall. Another approach proposed at the early age of fusion research [3] is to modify the topology of the external magnetic field to create a magnetic separatrix between the open and closed flux surfaces (see Fig. 1.4).

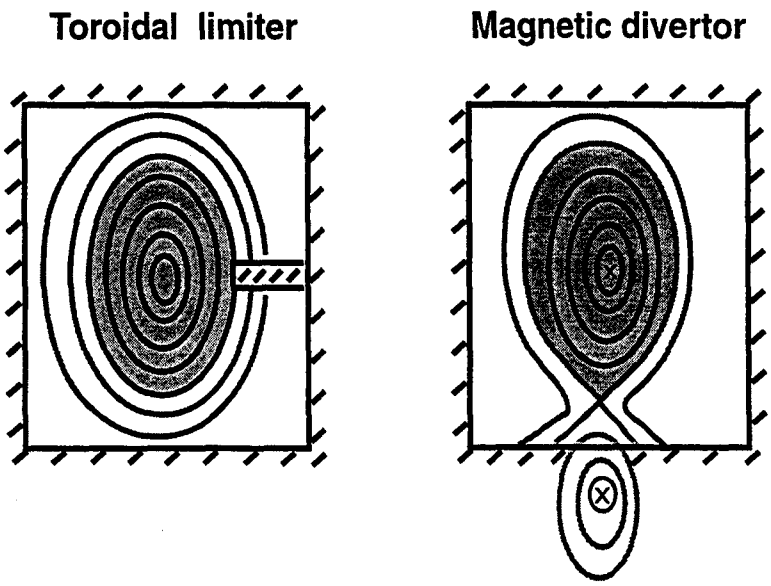

Figure 1.4: Limiter configuration vs. magnetic divertor

Chapter 2

Edge plasma in a divertor tokamak

2.1 Subject of the edge plasma

In the core region of the plasma magnetic surfaces close on themselves. Charged particles move mainly along the field lines and thus are confined to the flux surfaces (however due to field curvature there is also a slow drift across flux surfaces). Also, due to anomalous transport and collisions, particles diffuse across flux surfaces. Outside of the last closed flux surface (LCFS) there are open flux surfaces that are in direct contact with material walls of the reactor. This region forms the plasma edge. Here charged particles are not confined, as in the core plasma, and in a short time they leave plasma by coming in contact with the wall due to rapid motion along field lines.

2.1.1 Importance of the edge plasma

There are several physics and technology aspects which make the edge plasma quite important for tokamak operation.

• The edge plasma forms the boundary of the core plasma and therefore it affects the

core. The edge plasma in a fusion reactor must carry out large fluxes of energy and α-particles without degrading the high temperature and density conditions required in the core plasma.

- The power density at the target plates must stay below technological limits.
- An important issue is impurity transport from the wall to the core plasma since impurities present in the core plasma cause significant energy loss through radiation, as well as dilution of the ion fuel. The edge plasma temperature, density and flow distributions should be optimized to prevent penetration of impurities into the core plasma.
- For efficient helium ash exhaust, the gas density must be sufficiently high at the pump port entrance.

Thus the design of the magnetic configuration and the geometry of plasma facing components play critical roles in a fusion reactor. Successfull design will require understanding and control of features of the edge plasma.

2.1.2 Geometry of a tokamak with magnetic divertor

For magnetic divertors there are double-null and single-null configurations depending on whether there are two x-points in the edge plasma (one at the top and one at the bottom) or only one. Here in the edge plasma there are the scrape-off layer region (SOL) and the private flux (PF) region (see Fig. 2.1).

2.2 Scrape-off layer

The first important process in the SOL is particle transport along field lines. In the direction parallel to the magnetic field, charged particles can stream freely, interrupted only by collisions with other particles. Thus transport along field lines is governed

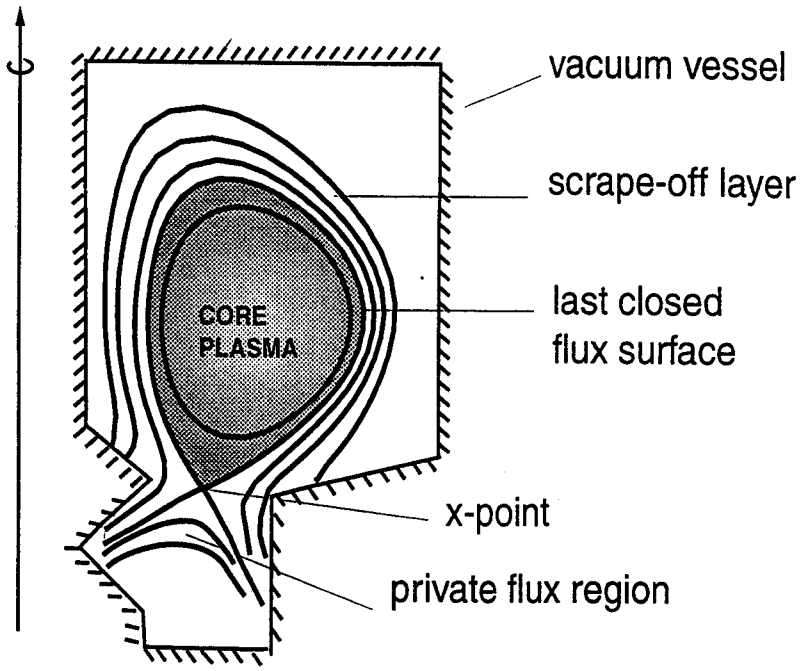

Figure 2.1: Poloidal cross-section of a tokamak with a magnetic divertor having a single x-point at the bottom

by collisions.

2.2.1 Collisional parallel heat transport

The Coulomb collision rate for electrons is

$$\nu_e \sim 4.5 \cdot 10^{-5} \frac{n}{T_e^{3/2}} \tag{2.1}$$

and the electron mean free path length is

$$\lambda_e \sim 1.5 \cdot 10^{12} \frac{T^2}{n} [cm] \tag{2.2}$$

where T is the electron temperature in eV, n is the electron density in cm^{-3}.

Electron-ion and ion-ion mean free paths are practically identical to this, within a factor of order of unity.

In collisional regime (i.e. in the regime where the mean free path length is much smaller than the characteristic size of the system) the parallel heat transport is local

$$q_{\|} = -n\chi_{\|}\nabla_{\|}T \tag{2.3}$$

Collisional heat conduction can be estimated as a random walk process

$$\chi_{\|} \sim D_{\|} \sim \lambda^2\nu \tag{2.4}$$

Thus the electron parallel heat conductivity is

$$\kappa_{\|} = n\chi_{\|,e} \approx n\lambda_e^2\nu_e \approx 2800\ T_e^{5/2}\ [Wm^{-1}eV^{-7/2}] \tag{2.5}$$

The ion heat diffusivity $\chi_{\|,i}$ is smaller than $\chi_{\|,e}$ by a large factor $\sqrt{M_i/m_e}$.

Usually validity of the collisional estimate implies that the collisional mean free path length is small compared to the temperature gradient scale length: $\lambda_e \ll L_T$. But the validity criterion for Eq. 2.3 is more stringent, since heat conduction is dominated by tail electrons with a velocity $\sim$ 3-4 V_{te} for which the mean free path length is $\lambda_{hc} \sim 5\lambda_e$ [4]. For steeper gradients, the heat flux is non-locally determined by a weighted mean of the temperature profile over a range of a few λ_e.

In C-Mod at the separatrix $n \sim 10^{14}\ cm^{-3}$ and $T \sim 50$ eV, thus $\lambda_e \sim 40$ cm. The connection length from plate to plate for an open magnetic field line in C-Mod is about 15 m. This seems to be large enough for validity of the local collisional heat transport model. However due to the strong temperature dependence in $\chi_{\|}$, most of the temperature drop occurs right at the plate where the parallel gradients are very

large. Thus at the plate the local collisional transport model is violated, and here kinetic corrections are required. Far from the plate, the local collisional transport model is valid for C-Mod.

2.2.2 Parallel plasma flow

The situation for the flow of particles is far more complicated than that for the flow of energy. Material surfaces, such as the target plates or the limiter, are sinks for particles, but there are also other significant sources and sinks in the plasma volume due to ionization and recombination. Presently there is no clarity in spatial distribution of particle sources and sinks in the tokamak edge plasma. The complexity of the parallel flow is illustrated by existence of reverse flows (away from the divertor in SOL) observed in many experiments [5, 6, 7]. However it is usually found that the particle flow in SOL is substantially subsonic ($M \lesssim 0.1$) [6, 7].

2.2.3 SOL profiles

The most basic experimental information about the edge plasma is in the measured profiles of plasma density $n_e(r)$ and electron temperature $T_e(r)$. It is generally known that these profiles decay in an exponential-like manner towards the wall. On C-Mod, the typical e-folding lengths are of the order of a few mm according to the measurements from a scanning Langmuir probe [6].

Temperature profile

The $T_e(r)$ profile can be used for estimating the cross-field heat diffusivity if one assumes that the cross-field heat flux is balanced by the [classical] parallel heat conduction.

The cross-field heat flux, $q_\perp$, is

$$q_\perp = (n_s \chi_\perp) \nabla_\perp T / \lambda_T \tag{2.6}$$

where λ_T is the width of the $T_e(r)$ profile, n_s is the plasma density at the separatrix and $\chi_\perp$ is the cross-field heat diffusivity.

For sufficiently high collisionality the parallel heat flux, $q_\parallel$, due to [classical] parallel heat conduction is

$$q_\parallel \approx \kappa_\parallel T_s / L_c \tag{2.7}$$

where $\kappa_\parallel$ is given by Eq. 2.5, T_s is the separatrix temperature, and L_c is the connection length along the field line from plate to plate. Eq. 2.7 implies that the target plate temperature is much smaller than the upstream temperature T_s (high recycling regime).

Assuming also that the volumetric heat loss is small the condition for the heat flux being divergence-free $\nabla \cdot \vec{q} = 0$ gives

$$q_\perp / \lambda_T + q_\parallel / L_c = 0 \tag{2.8}$$

Combining Eq. 2.6, 2.7, 2.8 together one arrives at a simple relation

$$\chi_\perp = \frac{\lambda_T^2 \kappa_\parallel}{n L_c^2} \tag{2.9}$$

For typical C-Mod edge parameters: $n_s \sim 10^{20}\ m^{-3}$, $T_s \sim 50$ eV, $\lambda_T \sim 5$ mm, $L_c \sim 15$ m Eq. 2.9 gives the value of $\chi_\perp$ about 0.05 m^2/s.

One should note that the electron temperature profile can be affected by energy exchange between electrons and ions. Simple calculations show that this effect becomes

important if temperature difference between the two species is larger than

$$\frac{\Delta T}{T} \approx 10^3(\lambda_e/L_c)^2 \tag{2.10}$$

As shown above in C-Mod $\lambda_e/L_c \sim 3 \cdot 10^{-2}$ and thus T_i and T_e must be different by a factor of $\gtrsim 2$ to make this effect significant.

Density profile

Neglecting the volumetric particle sources and sinks one can get an estimate of the cross-field particle diffusion coefficient $D_\perp$ in the SOL from the density profile $n_e(r)$, assuming simply that the radial particle flux $\Gamma_\perp$ is balanced by the parallel flow to the divertor:

$$(D_\perp \frac{n_s}{\lambda_n})/\lambda_n = n_s v_\parallel / L_c \tag{2.11}$$

or

$$D_\perp = \lambda_n^2 v_\parallel / L_c \tag{2.12}$$

Assuming the characteristic Mach number of the flow $M \sim 0.1$ for C-Mod parameters $L_c \sim 15$ m, $T_s \sim 50$ eV, $\lambda_n \sim 5$ mm this gives $D_\perp \approx 0.05\ m^2/s$ in agreement with the previous estimate for $\chi_\perp$ (Eq. 2.9).

2.2.4 Collisional cross-field transport

For the collisional cross-field transport the step size is the gyro-radius ρ. Then the classical cross-field heat difusivity is

$$\chi_\perp \sim D_\perp \sim \nu \rho^2 \tag{2.13}$$

Simple geometry arguments show that like-particle collisions produce no net diffusive

flux so it is the electron-ion collision frequency that enters here. Since the collision frequency is proportional to $T^{-3/2}$ while $\rho^2 \propto T$, perpendicular diffusion decreases with temperature:

$$\chi_\perp \sim D_\perp \propto T^{-1/2} \tag{2.14}$$

unlike the $T^{5/2}$ dependence of $\chi_\parallel$.

For a numerical estimate of the cross-field collisional transport, combining the electron-ion collision frequency with the electron gyroradius squared gives

$$\chi_\perp \sim D_\perp \approx 3 \cdot 10^{-4} \frac{n}{\sqrt{T} B^2} \tag{2.15}$$

where again T is in eV and the rest in cgs units.

For typical parameters in the edge plasma in C-Mod: $n \sim 10^{14} cm^{-3}$, $T \sim 50$ eV, $B \sim 5 \cdot 10^4$ Gauss this gives collisional cross-field transport coefficients of the order of a few cm^2/s. However toroidal effects enhance significantly the classical (collisional) transport according to the neoclassical theory [2]. In the highly collisional Pfirsch-Schluter regime [2] (which is certainly the case in the SOL in C-Mod) the neoclassical cross-field transport coefficients turn out to be greater than those in the slab geometry (as given by Eq. 2.13) by a factor of $\sim q^2/2$ where q is the safety factor; q is about 2-4 at the edge. However this is still not enough to account for the observed level of transport. Detailed modeling studies of these effects showed that the neoclassical transport still leads to underestimate of the measured cross-field transport rates [8].

2.2.5 Anomalous cross-field transport

As experimental radial SOL temperature profiles indicate that the level of cross-field transport greatly exceeds the classical transport the cross-field transport is anomalous i.e. caused by collective phenomena and turbulence rather than by particle collisions.

There are two different mechanisms through which the anomalous transport can arise: magnetic field fluctuations and electric field fluctuations. (In the literature they are often **incorrectly** called "electromagnetic" and "electrostatic" fluctuations. Electromagnetic effects may or may not be important for the turbulence mechanism but this has nothing to do with the question of whether it is $\tilde{E}$ or $\tilde{B}$ fluctuations that cause the anomalous transport.)

The magnetic field fluctuations destroy the nested structure of the magnetic flux surfaces by creating domains of overlapping magnetic islands (also called "magnetic flutter"or "stochastic layer"). Magnetic fluctuation give rise to radial particle flux [8]

$$\Gamma_{\perp}^{M} = \langle \tilde{n} v_{\parallel} \frac{\tilde{B}_r}{B} \rangle, \tag{2.16}$$

radial convected heat flux

$$q_{conv}^{M} = \frac{5}{2} T \Gamma_{\perp}^{M}, \tag{2.17}$$

and radial conducted heat flux

$$q_{cond}^{M} = -n\chi(\tilde{B}_r)\frac{dT}{dr}, \tag{2.18}$$

where brackets <> denote time-averaging over many fluctuations, $\chi(\tilde{B}_r)$ is model dependent [8]

However the magnetic field fluctuations are believed to play a minor role in the edge plasma according to experimental [9, 10, 11] and computational [12] studies.

Electric field fluctuations can drive particle flux by the $E \times B$ drift. There are several review papers on edge transport due to electric fluctuations; a recent one is by Endler [13].

The radial particle flux due to $\tilde{E}$ fluctuations is [8]

$$\Gamma_{\perp}^{E} = \langle \frac{\tilde{n}\tilde{E} \times B}{B^2} \rangle \tag{2.19}$$

radial convected heat flux

$$q_{conv}^{E} = \frac{5}{2} T \Gamma_{\perp}^{E} \tag{2.20}$$

and radial conducted heat flux

$$q_{cond}^{E} = \frac{5}{2} \langle n \frac{\tilde{T}\tilde{E} \times B}{B^2} \rangle \tag{2.21}$$

It was found in some experiments [14] that the global particle confinement time is in reasonable agreement with particle fluxes calculated from measured $\tilde{n}$ and $\tilde{E}$ fluctuations. The problem of establishing whether the heat loss is in agreement with fluctuation induced heat flux is more complicated than it is for particle transport. There is less published information on this matter and the situation remains less conclusive.

2.2.6 Theoretical models of edge plasma turbulence

Models for turbulence in the SOL are based on those from core turbulence but with added effects arising from the presence of limiter or divertor plates, namely that the field lines are open and there is a sheath boundary condition to be imposed at these plates [15]. In theoretical analysis it was found that the edge turbulence can be driven by interchange instability [16], resistive ballooning instability and non-linear drift wave instability [17], ionization drift instability [18], radiation driven modes [19], and by other mechanisms.

The comparison of various theories with the experimental scaling of transport coefficients is not very encouraging. There are several reasons. First, it is likely that many

effects together have to be included (temperature and density fluctuations, gradients and curvature of the magnetic field, electromagnetic effects, electron inertia, sheath boundary conditions, radial electric field) to quantitatively reproduce the observed fluctuations characteristics and induced transport. Second, there is evidence that the transport in the SOL may not be diffusive and analysis of large scale convective processes may be necessary. Third, some of the edge turbulence may come from propagation of turbulence from the core.

Thus more comprehensive non-linear computer simulations are needed to determine the features of the edge turbulence. Results from such numerical modeling of edge transport were presented in several reports [12, 20, 17]. These calculations are rather involved, still presently the most sophisticated computer simulations are not in a good quantitative agreement with the experimental data.

Thus, we presently have some **qualitative** understanding of the mechanism of the anomalous transport in the edge plasma but still there is no analytic theory, nor a computer model that would describe **quantitatively** the results inferred from experiments.

2.2.7 Empirical scaling of edge transport

If, even without a complete theoretical understanding, we had empirical knowledge of the features of the edge transport this would be sufficient to design next generation fusion devices. This motivated database studies of edge plasma parameters [6, 21, 22, 23, 24]. A comprehensive statistical investigation of measured density and temperature profile widths, λ_n and λ_T, for a group of major tokamaks was recently undertaken [23]. In particular it was found in [23] that in the low-recycling regime (defined there loosely as the regime with the separatrix electron temperature $T_{es} \gtrsim 50$ eV) in all machines the general trend is $\lambda_n, \lambda_T \propto (A_{LCFS}/I_p)^{0.7}$, where A_{LCFS} is the

surface area, while in the high-recycling regime (i.e. for $T_{es} \lesssim 50$ eV) the widths increase rapidly with increasing separatrix temperature T_{es}. This approach helps in illuminating trends more dedicated experiments are needed to provide a reliable extrapolation to larger machines.

In a different, perhaps more "physical", approach [24] twenty-one theoretical models of edge transport were considered, including those based on the effects of resistivity on ballooning and interchanges modes, drift turbulence, temperature gradient instabilities [15]. These models were tested on consistency with transport coefficients inferred from existing data. Some of these models indeed appear to fit better the data, and this perhaps may elucidate the underlying physics. Still the fits to data presented in that work [24] are far from being very convincing.

2.3 Divertor

In a divertor the LCFS is defined solely by the magnetic field and plasma surface interactions are remote from the confined plasma. There are several ways in which impurities can be produced: by interaction of ions and neutral particles with the wall, by evaporation due to high heat load, or by arcing. In the divertor configuration impurities released from the target are ionized and may be swept back to the target by the plasma flow before they can reach the LCFS and enter the confined plasma. However the advantage of divertor configuration in achieving cleaner plasma than those achieved in the limiter configurations still remains to be confirmed [25, 8]. Still the divertors have a clear advantage in achieving high gas compression which is allows to pump helium ash, and in radiating power though atomic processes which alleviates the heat load on the plasma facing components.

2.3.1 Impurity production

Physical and chemical ion sputtering is the most significant source of impurities in a fusion reactor [8]. Physical sputtering is the removal of atoms from the surface of the of a solid as a result of impact by ions or atoms. In general there is a threshold energy E_T, of the incident ion below which physical sputtering cannot occur [2]. Since E_T tends to be higher for materials with higher atomic mass the optimal choice for plasma facing components can be a material with a rather high Z (such as molybdenum in the case of Alcator C-Mod).

In chemical sputtering the wall material is eroded through chemical binding with hydrogen and other present substances. Chemical sputtering does not have a power threshold.

2.3.2 Plasma sheath

The most important feature of interaction of plasma with an absorbing surface is the development of an electrically charged layer at the surface. Generally in plasma the electrons have much larger thermal velocity than the ions. Therefore when plasma is in contact with an absorbing surface an electric field builds up to maintain plasma neutrality by repelling faster electrons. The principal potential drop is $\delta\Phi \approx 3T_e/e$ and it is located in a narrow region, the sheath [26].

The sheath thickness is of the order of several Debye lengths: $\lambda_D \approx 7.43\times10^2 T^{1/2} n^{-1/2}$ where T is in eV, otherwise cgs unit used. For typical parameters in the edge plasma in C-Mod $n \approx 10^{14}\ cm^{-3}$, $T \approx 10$ eV one finds $\lambda_D \approx 10^{-4}$ cm, thus the sheath is very thin. A small electric field, the presheath, extends more deeply into plasma. Due to the presheath ions are accelerated towards the sheath and as a result plasma enters the sheath at the sound speed.

The energy of plasma ions reaching the surface is determined by their thermal energy

and the sheath potential through which they fall. Since ion impact on surface can cause sputtering which depends strongly on the ion energy the sheath has a strong effect on impurity production and thus on overall performance of a fusion reactor.
The sheath also influences the flow of power to a surface. The power flux to the surface can be written

$$P = \gamma_s \Gamma T \tag{2.22}$$

where Γ is the ion flux density and γ_s is the sheath power transmission coefficient. The factor γ_s is approximately 6.5 for a hydrogen plasma with $T_i = T_e$ and no secondary electron emission [2]. If there is secondary electron emission the factor γ_s can be significantly enhanced.

2.3.3 Recycling and refueling

In most tokamaks the pulse length is many times larger than the particle replacement time [8]. Thus on average each plasma ion many times comes to the target plate and returns to the plasma during discharge. This process is called recycling.
When a plasma ion arrives at a solid surface it undergoes a series of elastic and inelastic collisions with the atoms of the solid. It may either be backscattered after one or more collisions, or slow down in the solid and be trapped. The trapped atoms can subsequently reach the plasma again after diffusion back to the solid surface. The ratio of the flux returning to the plasma from the solid, to the incident flux, is called the recycling coefficient.
The backscattering of ions incident on a surface depends primarily on the ion energy and on the ratio of the masses of the surface atom and the incident atom. The particles that are backscattered are predominantly neutral. The average energy of the backscattered particles is typically 30-50 % of the incident energy.
The hydrogen atoms that have been absorbed by the solid can be trapped, otherwise

they are released from the surface usually having thermal energies characteristic of the solid surface.

In a long discharge the plasma facing components attain an equilibrium where they return neutral particles at the same rate as they absorb ions. This is the case of complete edge refueling. However for achieving fusion conditions a peaked density profile may be more favourable. This can be achieved by core refueling using pellets of frozen hydrogen or neutral beams.

2.4 H-modes

For divertor tokamaks subject to strong auxiliary heating, two regimes with different confinement time can exist at about the same operating conditions. These regimes are dubbed L-modes and H-modes for low and high energy confinement. The mechanism for achieving the H-mode is still not entirely understood. The key parameter for getting into the H-mode is a sufficiently large input power although the power threshold depends on B_T, $\bar{n}_e$, the heating method, and some other parameters. Apparently the existence of an x-point is favourable for reducing the anomalous transport, as the H-modes are (with very few exceptions) found only in divertor tokamaks.

The H-mode is characterized by steep density and temperature gradients just inside the separatrix. Thus in the H-mode the anomalous transport coefficients near the edge are reduced dramatically.

2.5 Edge plasma studies in Alcator C-Mod

Alcator C-Mod is a compact tokamak (major radius of plasma $R = 0.68$ m), with a high magnetic field (5 Tesla and more), capable of producing shaped divertor plasmas. Its unique (for a machine of such class) feature is its molybdenum plasma facing com-

ponents and a closed divertor geometry. The core plasma density routinely achieved in C-Mod is $n \approx 4 \times 10^{20}\ m^{-3}$. Additional heating is supplied by ICRH.
A cross-sectional schematic diagram of C-Mod is shown in figure 2.2.
Alcator C-Mod has a variety of edge plasma diagnostics including two scanning Langmuir probes providing plasma density and temperature measurements across the SOL, a set of stationary Langmuir probes on the target plates providing plasma density and temperature measurements at the targets plates, bolometers providing radiated power data, a Thomson scattering system measuring plasma density and temperature across the SOL and inside the LCFS, and some other diagnostics.

2.6 Current problems in edge physics

In conclusion of this chapter the author would like to mention some highest priority problems in the edge physics today as it is presently viewed in the edge plasma community [25].

- What is the scaling of the anomalous $\chi_\perp$?
- Is there a significant contribution to cross-field heat transport due to convection?
- What role do the ions play in the flow of power?
- Is the parallel electron heat transport collisional or are kinetic effects important?
- What determines the radial density distribution in the edge plasma?

And specifically for Alcator C-Mod an important question is

- What is the mechanism of the core plasma fueling?

To address these questions the author has conducted an investigation of edge transport in the Alcator C-Mod tokamak, which is described further in the present thesis.

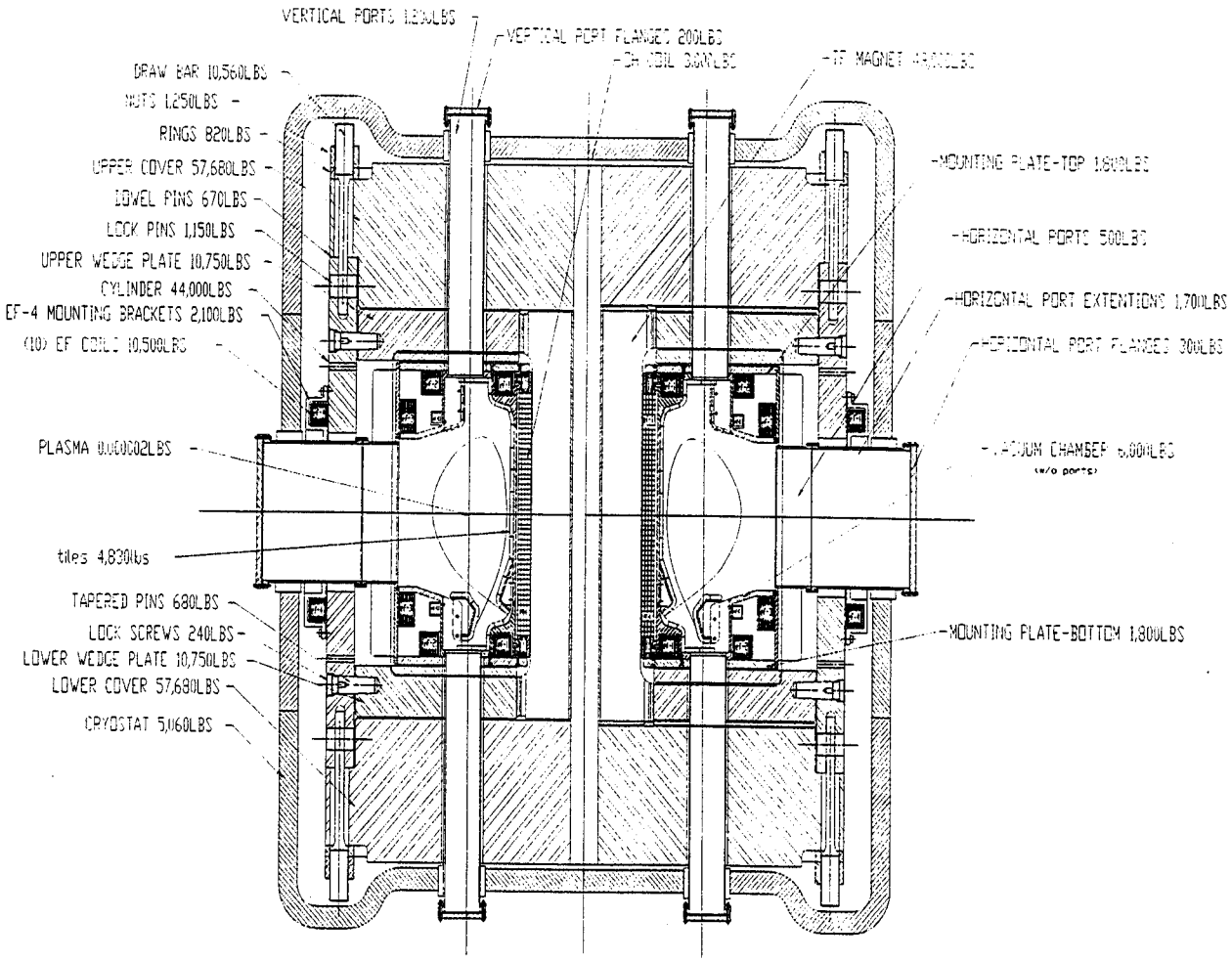

Figure 2.2: Cross-section of the Alcator C-Mod tokamak.

Chapter 3

Analysis of cross-field heat diffusivity in the SOL

The power width in the edge plasma is one of the most critical parameters of a fusion reactor since it determines the magnitude of the heat flux density that has to be accommodated by the divertor. The power width depends on the anomalous cross-field thermal diffusivity $\chi_\perp$ in the edge plasma. The value of $\chi_\perp$ can be estimated from the experimental SOL temperature profile using Eq. 2.9. This kind of estimate generally gives a numerical value in the range $0.05 - 1\ m^2/s$ for C-Mod and other tokamaks [25].

This simple way of estimating $\chi_\perp$ does not take into account the two-dimensional effects. A more rigorous approach is to use one of the existing edge codes (such as UEDGE, B2, EDGE2D etc.) and by matching experimental SOL T_e profiles infer a value of $\chi_\perp$ [27, 28].

However to design next generation fusion devices one needs to determine how $\chi_\perp$ scales with main parameters of the reactor such as plasma density, temperature, magnetic field strength etc. In order to infer such scalings a systematic study has to be undertaken for a large number of discharges over a broad range of parameters.

Such a study is not practical using the large existing edge plasma codes, which contain very detailed physics models and accurate treatment of geometry, however running these codes is difficult and modeling even a single discharge requires much time (many hours or days).

Another way to extract information about anomalous transport in the edge plasma is the "interpretive" approach. Here a simpler model is used, drawing on as much data as possible directly from the experiment. To address the problem of analysis of $\chi_\perp$ in the edge plasma for a large number of discharges a new code, EDGEFIT, has been developed by the author. This code combines the high speed of an interpretive code with accurate 2-D treatment of the real geometry.

3.1 Model description

The simplest model for the cross-field heat transport in the SOL is to assume that the anomalous heat flux is diffusive

$$q_\perp = -n\chi_\perp \nabla_\perp T \tag{3.1}$$

with $\chi_\perp$ being the anomalous heat diffusivity.

This $\chi_\perp$ has the meaning of an "effective" thermal diffusivity. If the cross-field thermal energy flux has a convective term, due to particle diffusion, then

$$q_\perp = -n\chi_\perp \nabla_\perp T - \frac{5}{2} T D_\perp \nabla_\perp n \tag{3.2}$$

then the effective $\chi_\perp$ can include both heat diffusion and convection:

$$\chi_\perp^{eff} = \chi_\perp + \frac{5}{2} D_\perp \frac{\partial ln(n)}{\partial ln(T)} \tag{3.3}$$

Similarly the effective χ can include a pinch term.

It is assumed that the heat flux in the direction along the field is given by the classical heat conduction

$$q_{\|} = -\kappa_{\|} \nabla_{\|} T \tag{3.4}$$

with the Spitzer heat conduction coefficient (Eq. 2.5)

$$\kappa_{\|} = 2800 \cdot T^{5/2} \ [Wm^{-1}eV^{-7/2}] \tag{3.5}$$

In the simplest model the source term (radiation) can be completely neglected here since radiation occurs mainly below the x-point level and thus should have only a small effect on the upstream radial T profile in SOL. However it can be kept for generality. Then the resulting equation modeling heat transport in the edge plasma is

$$\nabla \cdot (\hat{e}_{\|} \kappa_{\|} \nabla_{\|} T + \hat{e}_{\perp} n \chi_{\perp} \nabla_{\perp} T) = P_{rad} \tag{3.6}$$

Although this equation looks quite simple it is not analytically solvable due to the non-linearity entering through the $\kappa_{\|}$ temperature dependence. Another problem is the complexity of the real geometry determined by the magnetic field and material boundaries.

3.1.1 Flux coordinates

Since the heat transport is anisotropic with respect to the direction of the magnetic field the natural choice of the coordinate system is the magnetic flux coorinates. We need to make the transformation from a cylindrical coordinate system (R, Z, ϕ) to a flux coordinate system (ψ, χ, ϕ) where we will choose the poloidal flux ψ as the generalized radial coordinate (see Appendix A), χ as the generalized poloidal angle

(taken orthogonal to $\nabla\psi$) and ϕ as the real toroidal angle.

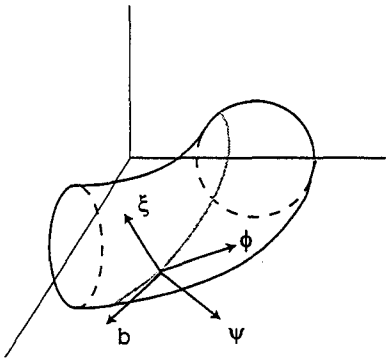

Figure 3.1: Principal directions. The ϕ coordinate is the toroidal angle, $\vec{b}$ is the normalized magnetic field vector, $\vec{\psi}$ is orthogonal to the flux surface, $\vec{\xi}$ is orthogonal to both $\vec{b}$ and $\vec{\psi}$.

The principal directions are defined by the following set of vectors (hat denotes a unit vector):

$$\begin{aligned} \hat{b} = \frac{B_\chi}{B}\hat{\chi} + \frac{B_\phi}{B}\hat{\phi} = \hat{e}_\parallel = b_\chi\hat{\chi} + b_\phi\hat{\phi} \\ \hat{\xi} = \hat{b}\times\hat{\psi} = b_\phi\hat{\chi} - b_\chi\hat{\phi} \\ e_\perp = \hat{\psi} + \hat{\xi} = \hat{\psi} + b_\phi\hat{\chi} - b_\chi\hat{\phi} \end{aligned} \tag{3.7}$$

The starting point for this coordinate transformation is to assume that we know the functional relationship between the original coordinates and the generalized coordinates

$$\begin{aligned} \psi &= \psi(R,Z), \\ \chi &= \chi(R,Z). \end{aligned} \tag{3.8}$$

The element of arc length ds is given by

$$(ds)^2 = g_{\psi\psi}(d\psi)^2 + g_{\chi\chi}(d\chi)^2 + g_{\phi\phi}(d\phi)^2 \tag{3.9}$$

where the g_{ij} are just the diagonal elements of the covariant metric tensor. Since we working with orthogonal coordinates there are only diagonal terms in the metric tensor and the elements of the contravariant metric tensor g^{ij} are easily related to the elements of the covariant tensor g_{ij} by $g_{ii} = 1/g^{ii}$ (no sum). The elements of g^{ij} are calculated from (3.8) as

$$\begin{aligned} g^{\psi\psi} &= \nabla\psi \cdot \nabla\psi = (RB_\chi)^2 \\ g^{\chi\chi} &= \nabla\chi \cdot \nabla\chi = \left(\frac{\partial\chi}{\partial R}\right)^2 + \left(\frac{\partial\chi}{\partial Z}\right)^2 \\ g^{\phi\phi} &= \nabla\phi \cdot \nabla\phi = \frac{1}{R^2} \end{aligned} \tag{3.10}$$

where $B_\chi = \nabla\psi \times \nabla\phi$ is the poloidal magnetic field. The volume elements transform with Jacobian which is the square root of the determinant of the metric tensor. Since we are working with orthogonal coordinates there are only diagonal terms in the metric tensor and the Jacobian is

$$\sqrt{g} = (g_{\psi\psi}g_{\chi\chi}g_{\phi\phi})^{1/2} = h_\psi h_\chi R = \frac{h_\chi}{B_\chi}$$

where $h_\chi \equiv \sqrt{g_{\chi\chi}}$ and $h_\psi \equiv \sqrt{g_{\psi\psi}}$. Now we need to express all of the needed differential operators in the flux coordinates. The gradient operator for a scalar is

$$\nabla A = \frac{1}{h_\psi}\frac{\partial A}{\partial\psi}\hat{e}_\psi + \frac{1}{h_\chi}\frac{\partial A}{\partial\chi}\hat{e}_\chi + \frac{1}{R}\frac{\partial A}{\partial\phi}\hat{e}_\phi, \tag{3.11}$$

The divergence of a vector is

$$\nabla \cdot \vec{A} = \frac{1}{\sqrt{g}}\left(\frac{\partial}{\partial\psi}(Rh_\chi A_\psi) + \frac{\partial}{\partial\chi}(Rh_\psi A_\chi)\right) + \frac{1}{R}\frac{\partial A_\phi}{\partial\phi}. \tag{3.12}$$

The heat diffusivity tensor in the (ψ, ξ, b) basis is diagonal

$$\hat{\chi} = \begin{pmatrix} \chi_\perp & 0 & 0 \\ 0 & \chi_\perp & 0 \\ 0 & 0 & \chi_\parallel \end{pmatrix}$$

Then in the axi-symmetric $(\partial/\partial\phi = 0)$ case our heat conduction equation (Eq. 3.6) becomes

$$\frac{\partial}{\partial\psi}\left(nC_1\frac{\partial T}{\partial\psi}\right) + \frac{\partial}{\partial\chi}\left(nC_2\frac{\partial T}{\partial\chi}\right) = \sqrt{g}P_{rad} \tag{3.13}$$

where

$$C_1 = \frac{Rh_\chi\chi_\perp}{h_\psi} \tag{3.14}$$

$$C_2 = \frac{Rh_\psi(b_\phi^2\chi_\perp + b_\chi^2\chi_\parallel)}{h_\chi} \tag{3.15}$$

3.1.2 Semi-analytic solutions

To obtain some insight on the the non-linear PDE (3.13) it is instructive to analyze a simpler non-linear PDE that has a similar form

$$\frac{\partial^2(T^{7/2})}{\partial s^2} + C\frac{\partial^2 T}{\partial\rho^2} = 0 \tag{3.16}$$

where ρ stands for the radial (flux) coordinate, s is the poloidal projection of the length along the magnetic line and the constant C lumps together all constant factors. Equation (3.16) corresponds to the slab model of the SOL with constant cross-field heat conduction $(n\chi_\perp)$. Consider the domain $\{\rho \geq 0;\ -1 \leq s \leq 1\}$ with boundary conditions

$$T(s=1) = T(s=-1) = 0; \quad T(\rho\to\infty) = 0 \tag{3.17}$$

Assume that there is a solution with separating variables: $T = R(\rho)S(s)$. Then solving for the radial part $R(\rho)$ one finds

$$R(\rho) = (\rho + \rho_0)^{-\frac{4}{5}} \tag{3.18}$$

where ρ_0 is a constant. This describes a non-exponential decay of the radial temperature profile.

The poloidal profile is given by

$$S(s) = \hat{S}(s)\,(C\frac{36}{25})^{\frac{2}{5}} \tag{3.19}$$

where $\hat{S}(s)$ is a solution of the following non-linear eigenvalue problem

$$\frac{d^2(\hat{S}^{\frac{7}{2}})}{ds^2} = -\hat{S} \tag{3.20}$$

with boundary conditions $\hat{S}(-1) = \hat{S}(1) = 0$.

The eigenvalue problem (Eq. 3.20) can be easily solved numerically by the shooting method [29] and the resulting $\hat{S}(s)$ profile is shown in Fig. 3.2.

Fig. 3.2 illustrates an important feature of the poloidal temperature profile in the SOL: temperature drops rapidly near the target plates and in the main SOL it remains relatively constant. This is a direct consequence of the non-linear parallel heat conduction ($\propto T^{5/2}$).

3.1.3 Computational approach

In the general case the non-linear PDE (3.13) has to be solved numerically on a computational mesh. It is sufficient to use a simple 5-point stencil (see Fig. 3.3) since there are no cross derivatives in Eq. (3.13) which is the advantage of solving the problem in orthogonal coordinates.

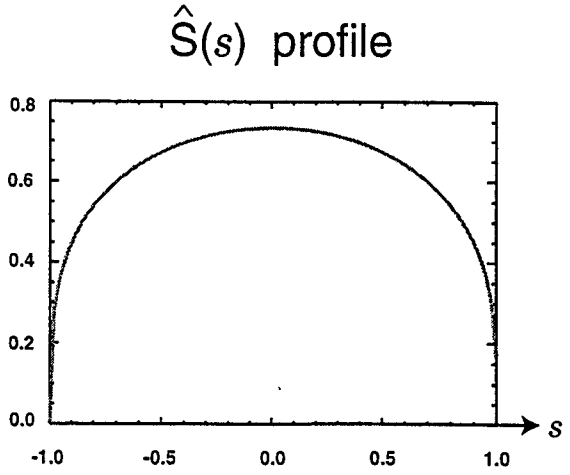

Figure 3.2: Numerical solution of the non-linear eigenvalue problem (3.20).

First the PDE is discretized using a conservative finite-difference scheme [30] which results in a system of N non-linear equations where N is the number of nodes in the mesh. This set of equations represents the constraints imposed on T values at each of the nodes of the mesh by the resulting finite-difference equation (for the internal nodes), or by boundary conditions (for the boundary nodes).

$$\begin{aligned} f_1(\vec{T}) &= 0 \\ f_2(\vec{T}) &= 0 \\ &\cdots \\ f_N(\vec{T}) &= 0 \end{aligned} \tag{3.21}$$

where $\vec{T} = \{T_1, T_2, ..., T_N\}$ is the ordered set of T values on the mesh.

Next, this set of equations $\vec{f}(\vec{T}) = \vec{0}$ is iteratively relaxed towards a solution by the

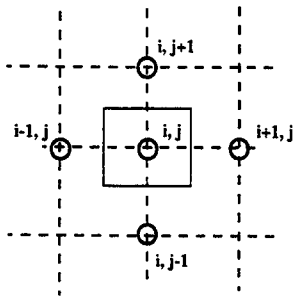

Figure 3.3: Computational "molecule" for solving Eq. (3.13) numerically by finite difference methods.

Newton's method [29]

$$\vec{T}^{n+1} = \vec{T}^{n} - (\frac{\partial \vec{f}}{\partial \vec{T}^{n}})^{-1} \vec{f}(\vec{T}^{n}) \tag{3.22}$$

At each iteration the set of equations is linearized, then the resulting sparse linear system is solved. Iterations are repeated until convergence is achieved.

For solving this problem the author developed a numerical code capable of solving a general non-linear elliptic PDE in arbitrary 2-D locally orthogonal coordinates. The code is written in IDL and FORTRAN and uses a standard direct (non-iterative) sparse linear solver from the IMSL library [31]. The geometry information in the form of $R(\chi, \psi)$ and $Z(\chi, \psi)$ is passed to the code which evaluates numerically the appropriate metric coefficients.

3.1.4 Test problems

Several sample problems have been run to test the code's performance. One such test was solving of Laplace's equation $\nabla^2 U = 0$ inside a torus with rectangular cross-sestion (Fig. 3.4).

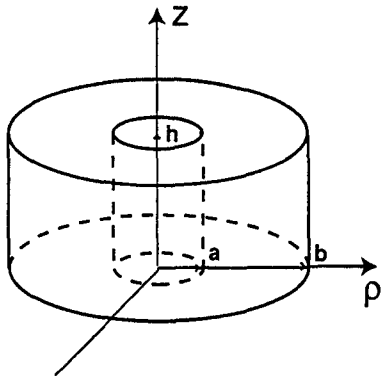

Figure 3.4: Geometry of the test problem. The Laplace's equation is solved numerically inside a torus with rectangular crossection.

With simple boundary conditions

$$U(z=0) = U(z=h) = U(\rho=a) = V_0;\ U(\rho=b) = V_0 + V_1 \tag{3.23}$$

the problem retains toroidal symmetry and has an analytic solution [32]

$$U(\rho,z) = V_0 + \frac{2V_1}{\pi} \times \tag{3.24}$$
$$\sum_{m=0}^{\infty} \frac{\sin\frac{\pi(2m+1)}{h}z}{2m+1} \times \frac{I_0\left[\frac{\pi(2m+1)}{h}\rho\right]K_0\left[\frac{\pi(2m+1)}{h}a\right] - I_0\left[\frac{\pi(2m+1)}{h}a\right]K_0\left[\frac{\pi(2m+1)}{h}\rho\right]}{I_0\left[\frac{\pi(2m+1)}{h}b\right]K_0\left[\frac{\pi(2m+1)}{h}a\right] - I_0\left[\frac{\pi(2m+1)}{h}a\right]K_0\left[\frac{\pi(2m+1)}{h}b\right]}$$

Here I_0 and K_0 are the zeroth order Bessel functions of imaginary argument of the 1st and 2nd kind respectively.

A numerical solution for a particular case: $h = 4, a = 1, b = 7, V_0 = 1, V_1 = 10$ is shown in Fig. 3.5. It appears to be very close to the exact solution given by Eq. 3.24. Several similar tests with sample linear and non-linear problems allowed the author to verify the code's performance.

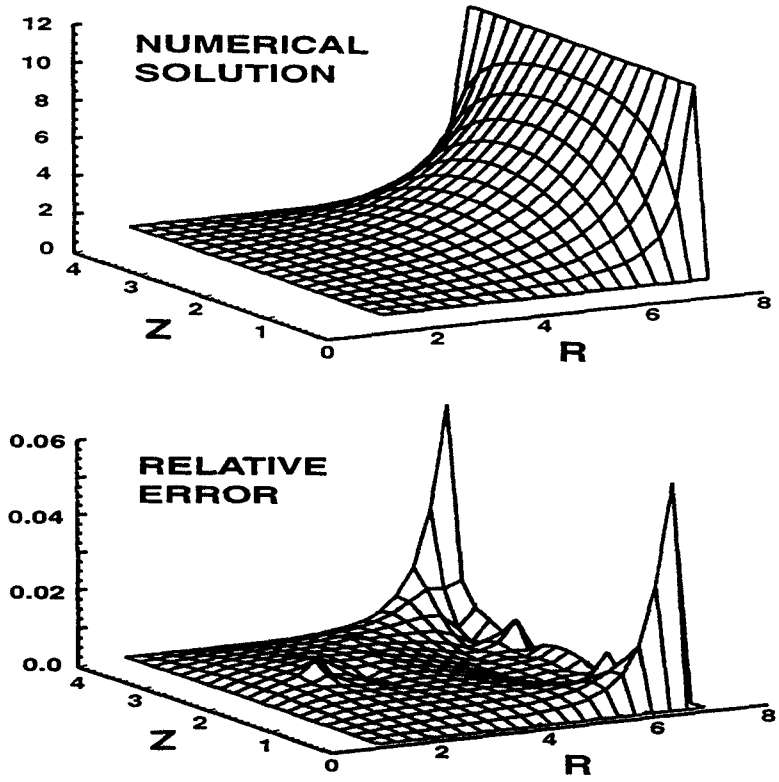

Figure 3.5: Numerical solution of Laplace's equation inside a torus with rectangular cross-section and the relative error defined as $|(T_{num} - T_{exact})/T_{exact}|$. The maximal error is about 6% and it appears in the corners where the boundary condition is discontinous.

3.1.5 Solving in the real geometry

In the real geometry case solving the heat conduction equation (Eq. 3.13) requires a computational mesh which follows the real geometry. For the edge plasma in C-Mod such a mesh is constructed by a grid generator program (developed by B.LaBombard) based on EFIT [33] magnetic reconstruction. An example of such a mesh is shown in Fig. 3.6.

The boundary conditions are specified according to the experimental data. Typically at the innermost boundary it is the value of the temperature or the heat flux, for

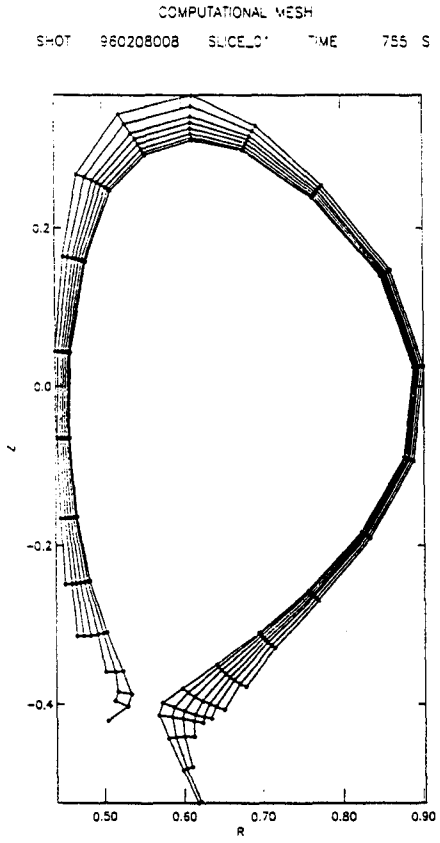

Figure 3.6: Computational mesh used for modeling of the edge plasma in C-Mod with the EDGEFIT code. A mesh is generated individually for a given shot and time slice.

the outermost boundary usually heat flux is set zero, and for the material boundary nodes the temperature is specified according to the measured temperature there.

3.2 Simulations and data analysis

3.2.1 Sensitivity studies

As expected, the calculated radial T profile is steeper with small $\chi_\perp$ and flatter for large $\chi_\perp$ (Fig. 3.7).

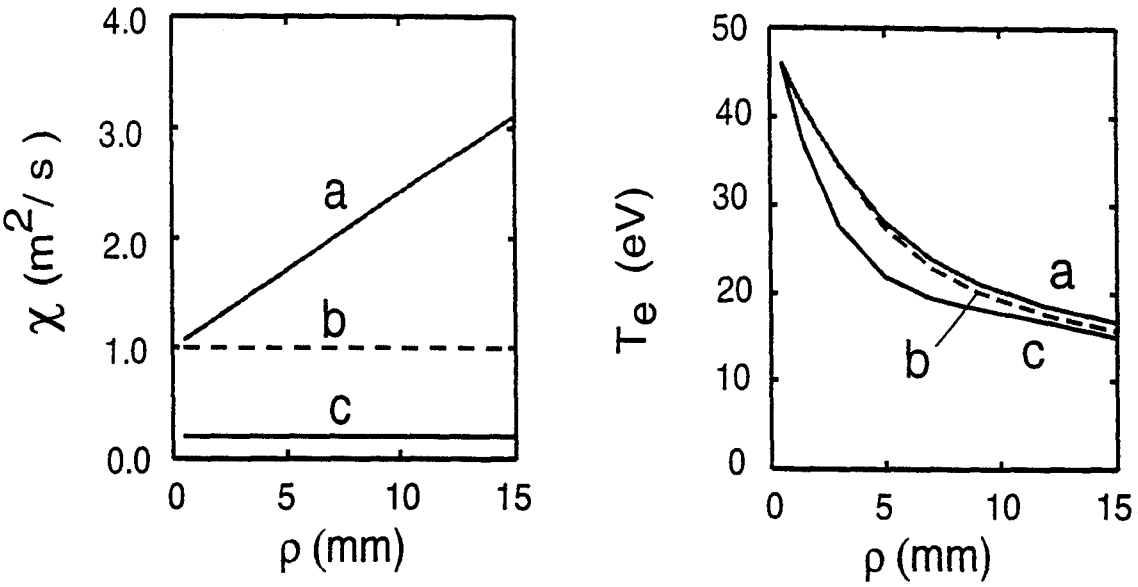

Figure 3.7: Three modeled radial $\chi_\perp$ profiles and three resulting radial T profiles. For smaller separatrix $\chi_\perp$ value the T profile is steeper. However the T profile is not sensitive to $\chi_\perp$ further out in the SOL ($\rho \gtrsim 5$ mm).

Solving the direct problem is finding a 2-D T profile on the mesh for a given $\chi_\perp(\rho)$ profile. Solving the inverse problem is finding the best matching $\chi_\perp(\rho)$ profile for a given radial T profile. An important feature of this problem found in simulations is that two very different $\chi_\perp(\rho)$ profiles can correspond to very similar $T(\rho)$ profiles. The T profile is relatively sensitive to the separatrix value of $\chi_\perp$, but not to the $\chi_\perp$ values further out into the SOL (Fig. 3.7). The main reason for this is that the plasma density profile is rapidly decreasing in the radial direction, and for a given density profile, the product $(n\chi_\perp)$ that enters (Eq. 3.6) depends mainly on the separatrix value of $\chi_\perp$. This property makes it difficult, if not impossible, to extract the whole radial profile $\chi_\perp(\rho)$ from the noisy measured radial T profiles. It appears that it is only the separatrix $\chi_\perp$ value, $\chi_{\perp 0}$, that can be found more or less reliably, and therefore only it is discussed further.

3.2.2 Fitting $\chi_\perp$ to data

From the experiment one has the electron temperature profiles across the SOL (measured by a scanning Langmuir probe [6]) and with this data one can find the $\chi_\perp$ best describing the experiment within the frame of our model.

In general a match with experimental Alcator C-Mod radial T profiles is obtained for $\chi_\perp$ in the range 0.1-10 m^2/s. The model allows us to match the experimental T profiles quite well; the fit error is usually about 1 eV per data point, which is just a few percent.

To make extraction of $\chi_\perp$ automatic in the code, in an external optimization loop, $\chi_\perp(\rho)$ is represented by a piece-wise linear function with several free parameters which are optimized to match the data. This solves the inverse problem of finding $\chi_\perp(\rho)$ from the measured temperature data. This external optimization is made by the downhill simplex method [29]. The optimization is completely automatic and takes just a few minutes on a DEC Alpha workstation. The code, combining an elliptic solver with an external optimization routine, was named EDGEFIT [22]. Hundreds of discharges have been analyzed by EDGEFIT, a task that would be impractical using a large predictive code (such as UEDGE, B2.5 etc).

3.2.3 Data analysis

EDGEFIT was run on a large number of Alcator C-Mod discharges and the calculated $\chi_{\perp 0}$ values were placed into a database containing a variety of information for each of the discharges. Regression analyses, with statistical tests of relevance and redundancy of regressors, were used to find what local (near separatrix) or global parameters could be responsible for variations of $\chi_{\perp 0}$. The database contains more than 500 time slices, mostly ohmic-heated L-modes. The range of core plasma density in the database is 0.5-2.8 10^{20} m-3, plasma current 0.4-1.1 MA, toroidal magnetic field 2.8-7.9 Tesla,

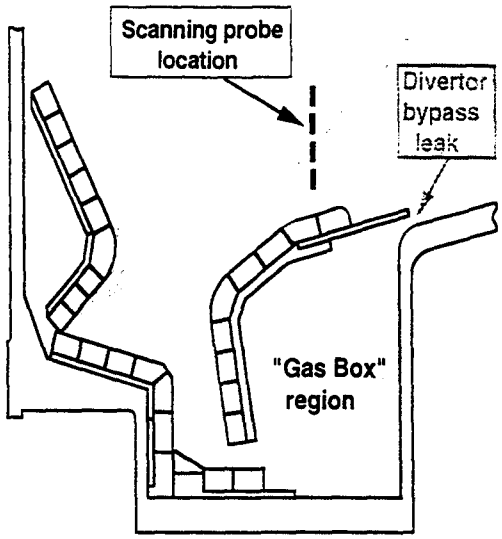

Figure 3.8: Neutral gas leak through the bypass in the Alcator C-Mod divertor.

separatrix temperature 20-80 eV, and safety factor (q_{95}) 3.0-7.4.

The whole data set consists of three subsets that were treated independently. These subsets correspond to the operation periods before and after July 1995 when a bypass leak of neutral gas was partially closed in Alcator C-Mod divertor (see Fig. 3.8), and after December 1996 when boron was first introduced in the Alcator C-Mod vessel [6].

It appears that the subsets corresponding to open and closed bypass have quite different $\chi_{\perp 0}$ values. For discharges with open bypass the inferred $\chi_{\perp 0}$ values are larger on average by a factor of about 3 than for those with bypass closed. This has been previously found from approximate onion-skin model analysis [6]. A neutral gas bypass leak in the divertor can probably cause a local perturbation of plasma temperature in SOL. This may be a possible explanation for this effect. There also a possiblity that this is an artifact caused by a systematic error in the FSP measurements.

Within each of the data subsets, a linear regression analysis was applied in search of a power law scaling for $\chi_{\perp 0}$ versus other parameters according to

$$ln\ (\chi_{\perp 0}) = C_0 + C_1\ ln(X_1) + C_2\ ln(X_2) + ... + C_N\ ln(X_N) \qquad (3.25)$$

where C_i are fitted constants and X_i are the independent variables. Various sets of plasma parameters were tested as independent variables X_i: core plasma density n_{core}, separatrix plasma density n_{sep}, separatrix plasma temperature T_{sep}, toroidal magnetic field B_{tor}, the safety factor q_{95}, the midplane neutral pressure P_{mid} and the divertor neutral pressure P_{bot}. The partial F-test [34] was used to find relevance and redundancy of regressors.

Some results of the statistical analysis are shown in Tables 3.1 and 3.2. Large value of the partial F-test in the tables (as compared to the 95% significance level which is roughly 3-6 in this case) would indicate that a particular regressor is relevant. Similar tables for $\chi_{\perp 0}$, tested against different regressor sets, were analyzed in the sense of backward elimination: going from the bottom to the top and eliminating those regressors that have the smallest partial F-values [34]. This procedure allows one to find a small set of regressors that describe the data almost as well as a complete model.

For our data it turned out that only single regressor models could be accepted. The values of $\chi_{\perp 0}$ appeared to be slightly correlated with the separatrix density, midplane neutral pressure, the bottom neutral pressure and with core plasma density. This can be seen from Table 3.1 for the case of open bypass and no boron. The plot in Fig. 3.9 also shows that $\chi_{\perp 0}$ values have a trend to decrease as the midplane gas pressure grows. A plot of $\chi_{\perp 0}$ values versus the separatrix density, core density or the bottom pressure would look similar to Fig. 3.9 since all these quantities are correlated with each other and with the midplane pressure, and therefore one of them can affect $\chi_{\perp 0}$

through any of the others.

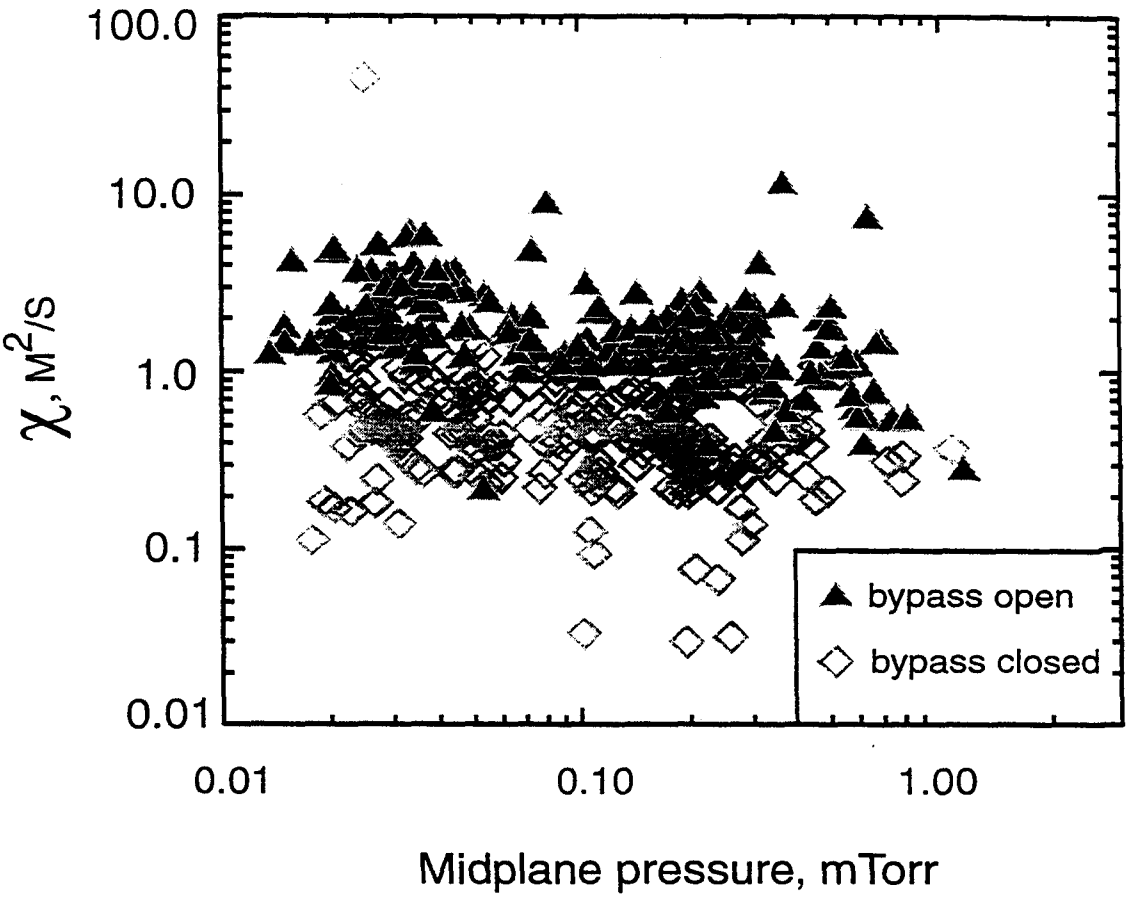

Figure 3.9: The $\chi_{\perp 0}$ values inferred by EDGEFIT from $\sim$ 500 C-Mod shots data are plotted against the mid-plane neutral pressure. With open bypass the $\chi_{\perp 0}$ values are by a factor of $\sim$ 3 larger than those with closed bypass.

For the toroidal magnetic field B_{tor}, the safety factor q_{95} and the local electron temperature T_{sep} no statistical correlation with $\chi_{\perp 0}$ was found for any of the three data subsets. This can be seen from Table 3.2 for the case of open bypass and no boron. This does not necessarily imply that these parameters have no effect on $\chi_{\perp 0}$, because

the influence of one parameter might be compensated by another one. Still statistical methods allow one to test a particular model containing these parameters for consistency with the data. As a special case, the Bohm scaling ($\chi_B \propto \frac{T}{B}$) was tested within each of the subsets. For this purpose the Bohm scaling was considered as a null hypothesis [35] to be tested against an alternative hypothesis which was taken as the best fit for $\chi_{\perp 0}$ with only temperature T and magnetic field B as regressors. The F-test with the data showed that the null hypothesis can be rejected at the 95% confidence level or, equivalently, the probability of incorrectly rejecting the null hypothesis is less than 5%. Thus there is a strong evidence that the Bohm scaling does not hold here.

3.2.4 Discussion and conclusions

The simple model of heat transport considered here allows us to obtain a good match with the experimental profiles of temperature in the SOL but the T profile is insensitive to the shape of the $\chi_\perp$ profile, only the separatrix value, $\chi_{\perp 0}$ is important. However the fact that a small gas leak from the divertor chamber to the main chamber has such a strong effect on the temperature profiles cannot be explained by our model. Moreover there is a significant disrepancy between the power coming to the edge plasma and the power conducted down to the target plates. All this suggests that a simple heat conduction model is not adequate to describe heat transport in the SOL. Unless there is a problem with the FSP data some physical effects related to the bypass may play a role here. Among important effects are: (i) radiation, (ii) heat loss by CX neutrals and (iii) radial convection of heat.

Radiation may be related to the bypass in some indirect way (impurity compression may change for example). However, the location where the FSP measurements are taken is higher upstream than the x-point and the divertor volume where radiation

occurs, thus it should not have a strong effect on the measured temperature profile. The effect of the divertor gas leak may be explained more simply by CX neutrals that are coming out of the divertor chamber through the bypass. This neutral flux enhances the cross-field heat loss in the ion-neutral channel, as this may perturb the measured temperature profile. Indeed, the CX contribution to the $\chi_\perp$ can be estimated from the random walk arguments as $\chi_{\perp CX} \sim (n_N/n_e)\lambda_{CX}V_{TN}$, where n_e and n_N are the plasma density and the neutral density, λ_{CX} is the neutral mean free path length, V_{TN} is the neutral thermal velocity. Generally, in C-Mod in the edge plasma $n_e \sim 10^{20}m^{-3}$ and temperature $T \sim 25$ eV for which the charge-exchange cross-section is $\sigma_{cx} \sim 3 \times 10^{-19}\ m^{-2}$ [36], thus λ_{CX} is of the order of 1 cm and V_{TN} can be estimated as $\sim 5\times10^6$ cm/s. As the inferred $\chi_\perp$ values are typically of the order of 0.1 m^2/s the CX effect becomes significant for neutral density $n_N \gtrsim 10^{16}\ m^3/s$. At the outer mid-plane the high neutral pressure indicates neutral densities of the order of $10^{17}\ m^3/s$ and more [37]. Thus CX neutrals should have a strong effect on the heat transport in the edge plasma in C-Mod which may explain the effect of opening of the bypass on the temperature profiles.

Another possibility is that opening of the bypass enhances the convective heat loss. It was estimated that the leakage through the open bypass, Γ_l, is of the order of $10^{22}\ s^{-1}$ [37]. The radially convected power in the SOL due to convection of this particle flux can be estimated for separatrix temperature $T_s \approx 50$ eV as $P_{conv} \sim \frac{5}{2}T_s\Gamma_l \approx 0.2 \times 10^6\ mW$. This is quite significant compared with the total power entering the SOL, P_{SOL}, which is of the order of 0.5-1.5 MW in C-Mod. Thus enhanced particle convection can be linked to the effect of opening of the bypass on the temperature profiles.

By the time of writing some data from the 1999 run campaign have become available. A controllable flap covering the bypass was operated in the 1999 run campaign [38] which allows to verify the older data from the 95-96 run campaigns. Some first

preliminary data from the new campaign show that there are slight changes in the n, T_e profiles as recorded by the F-port scanning probe, but they are not as dramatic as one would expect if one thought that the bypass alone was responsible for the differences previously seen in the 95-96 run campaigns [39]. At the time of writing it is thought that there was some other parameter that changed between 95 and 96 run campaigns; possibly the impurity levels or even the way in which the probe was operated [39].

Thus the study of anomalous heat diffusivities in SOL presented in this chapter points to either a problem with the FSP T_e data or some yet unknown physical parameter that has a dramatic effect on the measured T_e profiles. However the ideas that effects of CX neutrals and/or heat convection may be involved motivated a more detailed investigation of these effects, as described further in this thesis.

Regressor set	Coefficient of determination R^2	Regression coefficients					Partial F-test for the hypothesis			
		A_0	A_1	A_2	A_3	A_4	$A_1=0$	$A_2=0$	$A_3=0$	$A_4=0$
X_1	0.1219	24.15	-0.52				26.6			
X_2	0.1906	-0.19		-0.23				45.21		
X_3	0.1876	0.63			-0.19				44.34	
X_4	0.1371	33.07				-0.70				30.50
X_1X_2	0.1921	3.82	-0.09	-0.21			0.36	16.59		
X_1 X_3	0.1878	2.14	-0.03		-0.21		0.04		15.49	
X_1 X_4	0.1419	32.27	-0.19			-0.50	1.08			4.45
X_2X_3	0.1951	0.16		-0.14	-0.08			1.77	1.06	
X_2 X_4	0.1908	-2.78		-0.25		0.06		12.68		0.05
X_3X_4	0.1878	2.87			-0.18	-0.05			11.93	0.05
$X_1X_2X_3$	0.1953	1.65	-0.03	-0.14	-0.08		0.04	1.76	0.74	
X_1X_2 X_4	0.1943	-3.06	-0.17	-0.25		0.22	0.83	12.36		0.53
X_1 X_3X_4	0.1879	3.07	-0.02		-0.18	-0.03	0.01		10.75	0.01
$X_2X_3X_4$	0.1957	-4.20		-0.15	-0.09	0.09		1.86	1.15	0.14
$X_1X_2X_3X_4$	0.1969	-4.08	-0.11	-0.17	-0.07	0.19	0.29	2.12	0.60	0.38

Table 3.1: Results from multiple linear regression for data set with no boron and open bypass. The number of samples is 194. Testing regression models $ln\ (\chi_{\perp 0}) = A_0 + \Sigma A_i\ ln(X_i)$ where $X_1 = ln\ (n_{sepx}[m^{-3}])$, $X_2 = ln\ (P_{mid}[mTorr])$, $X_3 = ln\ (P_{bot}[mTorr])$, $X_4 = ln\ (n_{core}[m^{-3}])$.

Regressor set	Coefficient of determination R^2	Regression coefficients					Partial F-test for the hypothesis			
		A_0	A_1	A_2	A_3	A_4	$A_1=0$	$A_2=0$	$A_3=0$	$A_4=0$
X_1	0.1219	24.15	-0.52				26.6			
X_2	0.0178	-1.10		-0.37				26.66		
X_3	0.0008	0.17			0.12				0.15	
X_4	0.0011	0.67				-0.20				0.21
X_1X_2	0.1293	22.39	-0.50	-0.24			24.46	1.62		
X_1 X_3	0.1343	27.94	-0.59		-0.51		29.45		2.72	
X_1 X_4	0.1243	24.80	-0.53			-0.29	26.88			0.52
X_2X_3	0.0181	-1.19		0.36	0.07			3.37	0.05	
X_2 X_4	0.0201	-0.68		0.38		0.29		3.70		0.44
X_3X_4	0.0044	0.65			0.30	-0.45			0.64	0.70
$X_1X_2X_3$	0.1424	26.21	-0.57	0.25	-0.52		27.53	1.79	2.89	
X_1X_2 X_4	0.1327	23.05	-0.51	0.26		-0.35	24.68	1.84		0.75
X_1 X_3X_4	0.1349	28.17	-0.60		-0.59	0.19	28.65		2.31	0.13
$X_2X_3X_4$	0.0230	-0.68		0.38	0.28	-0.52		3.62	0.58	0.97
$X_1X_2X_3X_4$	0.1426	26.38	-0.58	0.25	-0.57	0.11	26.35	1.70	2.17	0.05

Table 3.2: Results from multiple linear regression for data set with no boron and open bypass. The number of samples is 194. Testing regression models $ln\ (\chi_{\perp 0}) = A_0 + \Sigma A_i\ ln(X_i)$ where $X_1 = ln\ (n_{sepx}[m^{-3}])$, $X_2 = ln\ (T_e[eV])$, $X_3 = ln\ (q_{95})$, $X_4 = ln\ (B_{tor}[Tesla])$.

Chapter 4

Analysis of particle balance in the edge plasma in C-Mod

A poloidal magnetic divertor could allow solution to the core contamination problem by physically separating the plasma-wall interaction zone from the confined plasma region and by allowing heat and particles in the scrape-off layer to flow into a remote chamber [40]. In this picture, it is assumed that the cross-field transport of heat and particles to the side wall is weak compared to the parallel transport, causing most of both particles and heat to flow along field lines and into the divertor chamber. In particular, particle balance in the core would be maintained by a back-flux of neutrals from the divertor into the core, in the absence of direct fueling by pellets or neutral beams. However, experimental observations of particle balance in the edge plasma and divertor of Alcator C-Mod [41] suggest that this picture can be overly simplified and in fact violated [42].

4.1 Particle balance observations

4.1.1 Relevant edge diagnostics

Among the edge plasma diagnostics in Alcator C-Mod, there are three used for inferring radial and poloidal particle fluxes in the edge plasma (see Fig. 4.1).

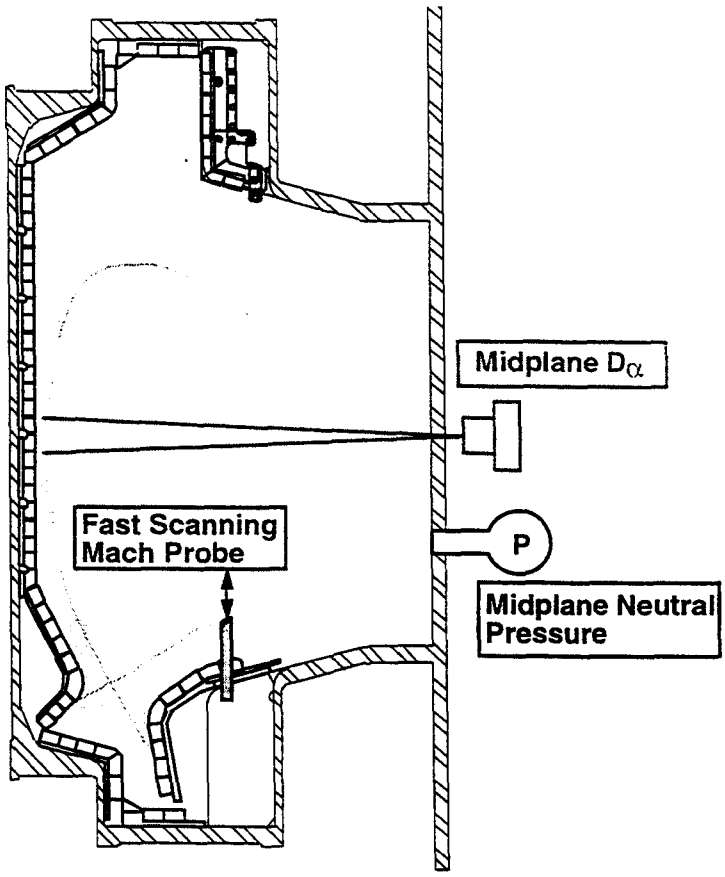

Figure 4.1: Data from depicted diagnostics are used for examining particle balance in the edge plasma in C-Mod

The poloidal ion flux in the SOL is inferred from the Mach probe located near the x-point level. The ion source in the edge plasma can be estimated on the basis of D_α brightness data. The inward neutral particle flux can be inferred from the mid-plane

neutral pressure measurements.

4.1.2 Poloidal flow strength from Mach probe

Alcator C-Mod is equipped with a scanning Langmuir (Mach) probe [6] which yields measurements of the plasma flow velocity in the outer SOL (see Fig. 4.1). The principle of this measurement is based on the fact that the potential drop in the presheath depends on the plasma flow velocity. In a plasma flow the "upstream" side of the probe (where the ions need less acceleration) faces a higher current density than the "downstream" side. For a Mach probe, the upstream and downstream sides are separated by an insulator; both currents are measured and the flow velocity is derived from the current ratio.

Measurements from the Mach probe indicate that parallel plasma flows into the divertor near the divertor throat have Mach numbers of no greater than $M \approx 0.1$. The main chamber and the divertor chamber communicate through a flux tube of width about $\delta\rho \approx 5$ mm at the midplane level. This yields an estimate of the total plasma flux entering the divertor chamber, Γ_{div}, for typical C-Mod parameters: upstream plasma density in the SOL $n \approx 10^{20}\ m^{-3}$, electron temperature $T_e \approx 50$ eV, major radius $R \approx 0.6$ m, and the pitch angle $\sin\phi \approx 0.2$:

$$\Gamma_{div} \approx 4\pi R \int_0^{\delta\rho} nV_{\|} \sin\phi \, d\rho \approx 4\pi R n V_{\|} \sin\phi \, \delta\rho \approx 6 \times 10^{21} s^{-1} \qquad (4.1)$$

4.1.3 Ion source from D_α brightness

Brightness of a spectral line is proportional to the population of the upper level of the corresponding transition. In particular in hydrogenic plasmas the population density of any excited level n can be expressed as

$$N_0^n = N_e[R_n(T_e, N_e)N_i + E_n(T_e, N_e)N_0] \tag{4.2}$$

where N_e, T_e are the electron density and temperature, N_i, N_0 are densities of ions and atoms in the ground state: the first term describes population resulting from recombination and the second term describes population from excitation of electrons in the ground state [43].

If either the recombination term or the excitation term in Eq. 4.2 dominates in populating of a certain level then the corresponding line radiation can be linked to either recombination rate or ionization rate. Using the numerical values of coefficients R_n, E_n tabulated in [43] one can estimate for conditions typical for the SOL in C-Mod: plasma density $n_e \lesssim 10^{14}\ cm^{-3}$ and neutral density $N_n \gtrsim 10^{10}\ cm^{-3}$, that recombination can contribute to D_α line radiation only for the temperature of the order of $\lesssim 1$ eV. Thus the plasma in the SOL in C-Mod is typically in the ionizing phase although in some rare cases significant recombination D_α radiation was observed at the mid-plane level due to MARFE [44].

The brightness of the D_α line (the first line of the Balmer series) radiation is commonly used to infer the ion source in plasma for hydrogen plasma in the ionizing phase [45]. The number of emitted D_α photons can be simply related to the number of ionization events according to detailed calculations [43]. The plot of the number of ionizations per emitted D_α photon is shown in Fig. 4.2.

From tomographic reconstructions of D_α emission, the magnitude of the plasma source inside the last-closed flux surface (LCFS) has been estimated in [46] to be in the range $S_{core} \sim 10^{21} - 10^{23}\ s^{-1}$. The spatial resolution of the tomography system is insufficient to resolve whether the ionization is truly inside or outside the LCFS and therefore S_{core} may be considered as a lower bound on the total ionization source in the main chamber.

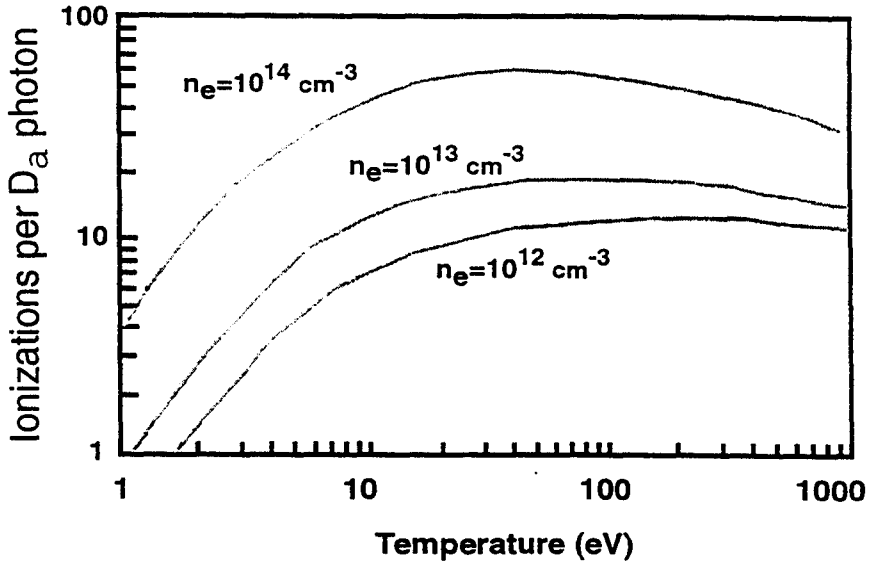

Figure 4.2: The number of ionizations per emitted D_α photon (after Johnson and Hinnov [41])

To analyze directly the D_α spectroscopy data, the author considered the brightness of a D_α signal measured at the midplane level (see Fig. 4.1) which corresponds to D_α emissivity integrated across the plasma. Although reflections of light from the walls may increase the apparent D_α brightness, this effect should be small here as the albedo of the interior walls in C-Mod for visible light is under 20% [47].

From chordal measurements of D_α brightness through the plasma midplane, B_α, the total ionization source in the main chamber can be estimated. Ionization events can occur in a rather broad range of densities and temperatures of the background plasma due to the spatial spread of the ionization zone and variation of conditions from one discharge to another. However the number of ionization per a D_α photon, N_α, does not vary too much and lies between 10 and 100 for plasma densities in the range 0.1-2.0 $\times 10^{20}$ m^{-3}, and electron temperatures, $20 - 200$ eV (see Fig. 4.2). The exact value of N_α within the indicated limits is not critically important for the conclusions

drawn here. For a simple estimate, it is assumed here that the effective number of ionizations per D_α photon is $N_\alpha \approx 45$ for all discharges. As the D_α brightness is usually found to be about the same for different chords viewing the upper half of the plasma, the D_α emissivity is probably more or less uniform poloidally in most cases. With photon energy, $E_\alpha \approx 2$ eV, and assuming a poloidally uniform distribution of emissivity over a narrow shell at the LCFS, the ion flux leaving the plasma per unit D_α brightness is roughly

$$\Gamma_i[s^{-1}] \approx \frac{1}{2} A_{LCFS}\, B_\alpha\, 4\pi\, N_\alpha\, \frac{1}{E_\alpha} \approx 6 \times 10^{21}\, B_\alpha\, [W/(m^2\, ster)]. \qquad (4.3)$$

4.1.4 Neutral inward flux from mid-plane pressure data

An ionization pressure gauge at the outer midplane of C-Mod (see Fig. 4.1) measures the density of molecules inside the gauge volume by ionizing the gas particles and measuring the magnitude of ion current arriving at a collector. This density is expressed in pressure units assuming that the gas inside the gauge volume is at room temperature. This is the "midplane pressure" which can be related to the density of neutral particles inside the vacuum vessel. However, since the neutral mean free path near the wall and inside the gauge is much larger than the gauge size, it is flux balance rather than pressure balance which is established between the gas inside the gauge and neutral particles inside the vacuum vessel.

As the neutral gas pressure measured at the top of the vessel is typically on the same order as that measured at the outer mid-plane, it seems reasonable to assume poloidal symmetry for gas distribution near the wall. Then the total neutral flux into the plasma can be estimated.

Typical midplane pressures in Alcator C-Mod are in the range 0.03-1.0 mTorr [37]. In steady state, the kinetic flux density of neutral atoms entering the plasma, $\frac{1}{4}n\bar{v}$,

also equal to the flux density of atoms entering the gauge, must be equal to 2 times the random flux density of molecules within the gauge.

Most likely inside the gauge there are only molecules at the room temperature since the incoming atoms suffer many collisions with the interior surface of the gauge by which they are trapped and thermalized. The average thermal speed $\bar{v} = (8T/\pi m)^{1/2}$ for D_2 molecules at room temperature is about 1200 m/s.

Using the Loschmidt's number $n_0 = 2.68 \times 10^{25}\ m^{-3}$ and the standard pressure $P_{st} = 760 \times 10^3\ mTorr$, the density of molecules inside the gauge (per one mTorr) is estimated as $n_{D2} = n_0/P_{st} \approx 0.35 \times 10^{20}\ m^{-3}/mTorr$.

For a LCFS area of $A_{LCFS} \approx 7m^2$, this leads to an estimate of the total neutral flux into the plasma per unit gauge pressure:

$$\Gamma_n[s^{-1}] \approx A_{LCFS}\,\frac{1}{2}(n_{D_2}\,\bar{v}_{D_2})_{gauge} \approx 1.6 \times 10^{23}\ P_{D_2}[mTorr]. \qquad (4.4)$$

4.1.5 Data analysis

The edge database of Alcator C-Mod features several hundred of representative discharges, with numerous diagnostic data recorded. Fig. 4.3 is a plot of the core ion flux estimated from measurements of main chamber D_α brightness using Eq. 4.3 versus midplane neutral pressure for a set of over 600 discharges.

The top secondary axis indicates the values of Γ_n from Eq. 4.4. In this data set the plasma current is 0.35-1.1 MA, the core plasma density is 0.7-4.8 $\times 10^{20}\ m^{-3}$ and the toroidal magnetic field is 2.8-7.9 Tesla. In Fig. 4.3 the dashed line is the estimated balance line where $\Gamma_i = \Gamma_n$. Divertor flux derived from experimental profiles and Eq. 4.1 is shown by cross symbols. H-mode and L-mode data from both diverted and inner-wall limited discharges are shown. The divertor flux shown on the same plot is clearly smaller than the core flux. The divertor flux is estimated for each discharge

from measured upstream profiles of plasma density and parallel velocity using Eq. 4.1 with an integration limit of $\delta\rho = 10$ mm.

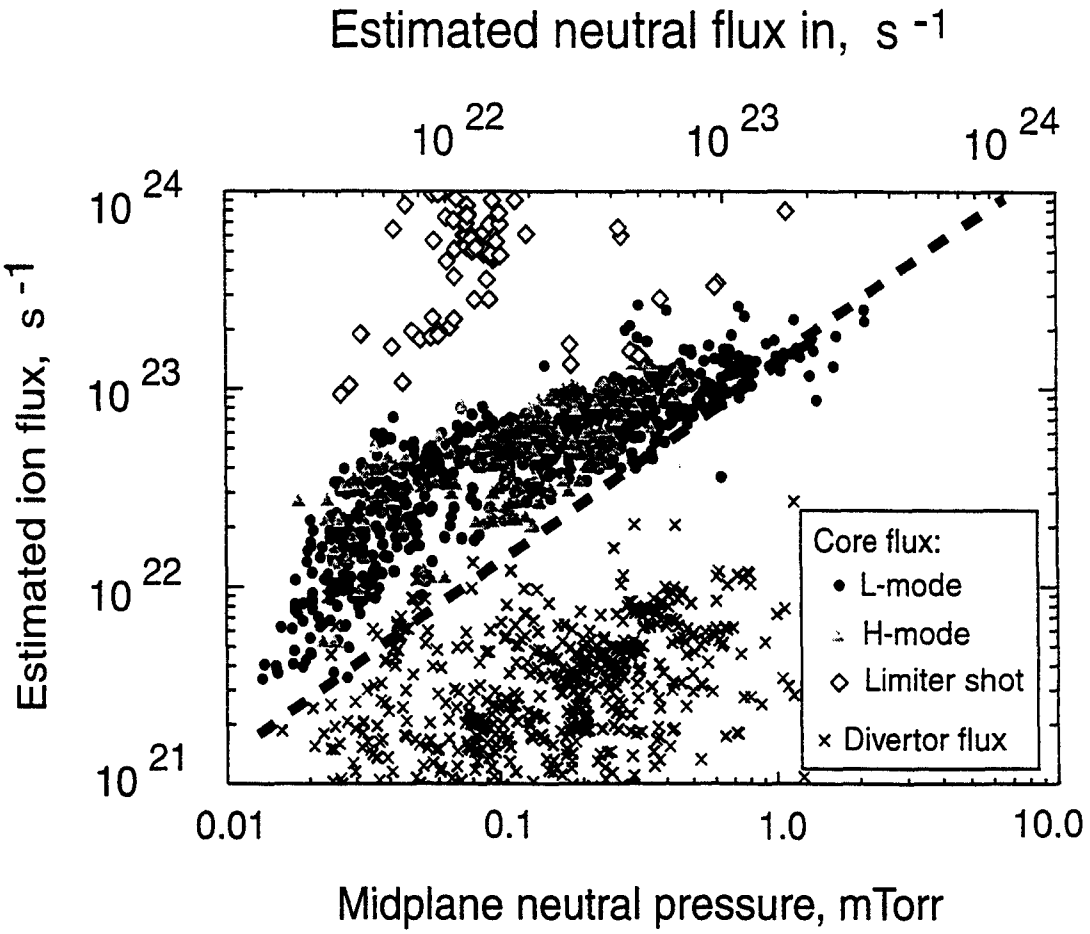

Figure 4.3: Core ion flux Γ_i derived from midplane D_α brightness using Eq. 4.3 is plotted against midplane neutral pressure.

One can see that for diverted discharges, the estimated neutral influx, Γ_n, is close to the estimated ion out-flux, Γ_i, over a range of two orders of magnitude.

Apparently systematic differences in Fig. 4.3 are due to poloidal non-uniformities in the D_α emissivities. The large discrepancy in limiter discharges shown in Fig. 4.3

exemplifies the latter effect. In this case, the intense, highly localized recycling light from the inner limiter surface is in the view of the detector.

The overall agreement between these two independent diagnostics in diverted discharges lends confidence to the ionization source estimates up to $S_i \sim 10^{23}\ s^{-1}$ in the main chamber.

4.2 Recycling pattern in C-Mod

When the estimate of the ionization source in the main chamber, S_{main}, based on data in Fig. 4.3, yields $S_{main} \sim 10^{23}\ s^{-1}$, it is clear that S_{main} is much larger than the total plasma flux into the divertor. The ionization source in the main chamber is thus balanced by plasma recycling on the main chamber walls rather than by plasma flow into the divertor (see Fig. 4.4).

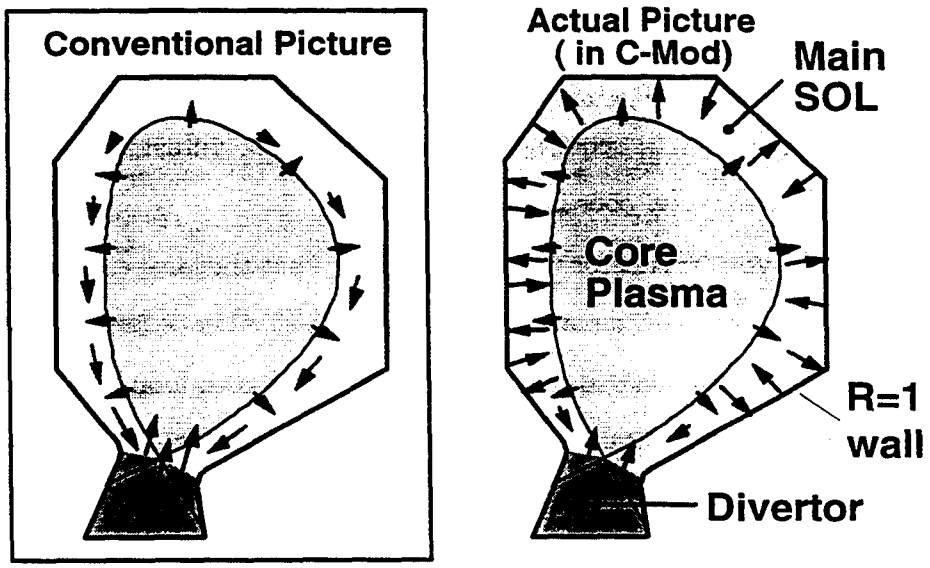

Figure 4.4: Recycling picture in C-Mod vs. the conventional picture.

The ionization source S_{main} is largest when the core plasma density is high. Thus, at least for high plasma densities ($n_{core} \gtrsim 10^{20}\ m^{-3}$), the particle balance in the main chamber primarily involves plasma flow to the main chamber walls balanced by radially inward neutral fluxes unlike the conventional picture where the radial outward flow is balanced by the poloidal flow to the divertor.

Although large recycling fluxes exist in the divertor chamber, they are apparently well separated from the recycling fluxes in the main chamber (see Fig. 4.4).

4.3 Implications

4.3.1 Anomalous cross-field particle transport

Accepting that the particle flow in the main chamber SOL at high densities is primarily radial, one is led to some important conclusions about anomalous cross-field particle transport in the SOL. If one assumes that the radial plasma transport in the SOL is diffusive i.e. $j_\perp = -D_\perp \nabla_\perp n$, then the positive curvature of the SOL plasma density profile (see Fig. 4.5) requires an effective plasma diffusion coefficient that grows rapidly with the radial coordinate.

It is observed in all types of Alcator C-Mod discharges that the local cross-field density e-folding length increases with distance from the LCFS [6]. Fig. 4.5 clearly illustrates this point, showing a nearly flat density profile for radial coordinates greater than 5 mm. Since volume recombination is negligible in these main chamber SOL plasmas ($T_e > 10$ eV), the radially-outward plasma flux must be lowest near the separatrix ($\rho = 0$ mm) and increase towards the wall. In order to drive even a constant flux, the effective cross-field diffusion coefficient must increase by more than an order of magnitude over the SOL profile. The radial profile of $D_\perp$ grows at least as $1/n_e(\rho)$ which, according to Fig. 4.5, gives for the ratio of $D_\perp$ values at ρ =15 mm and at

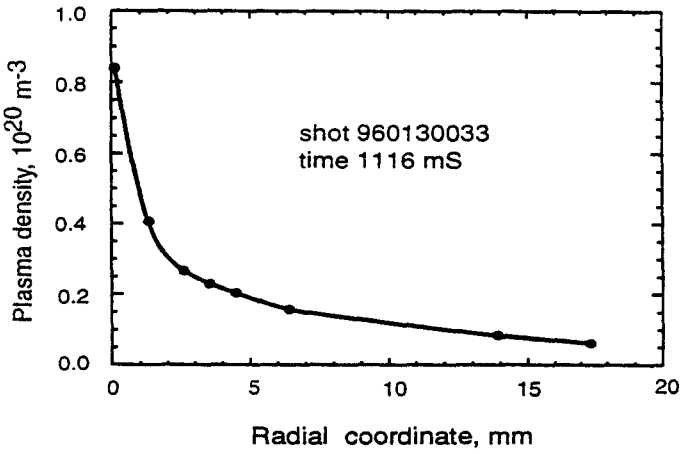

Figure 4.5: A typical plasma density profile in Alcator C-Mod has a flat 'shoulder' far in the SOL which, for the radial balance picture, requires very large anomalous diffusion coefficient.

the separatrix, $D_{\perp 15}/D_{\perp 0} \gtrsim 10$.

The spatial resolution of the D_α measurements is insufficient to determine how many ionizations occur inside the LCFS rather than in the SOL. However, the ionization mean free path for neutrals in the SOL in C-Mod is on the order of 1 cm which is comparable to the width of the SOL. Therefore recycling neutrals have a significant probability of ionizing inside the LCFS.

If the fraction of neutrals penetrating inside the LCFS is $\xi \approx 0.3$ then for the total ionization source in the main chamber, $S_i \lesssim 10^{23}\ s^{-1}$, the plasma out-flux from the core is $\Gamma_{core} \approx \xi S_i \lesssim 0.3 \times 10^{23}\ s^{-1}$.

Then the effective diffusion coefficient, $D_\perp$, can be estimated near the separatrix from the e-folding length of the density profile, $\lambda_n \approx 3\ mm$ and plasma density $n \approx 10^{20}\ m^{-3}$ as

$$D_\perp \approx \frac{\xi S_i / A_{LCFS}}{n/\lambda_n} \lesssim 0.1\ m^2/s. \tag{4.5}$$

For H-mode plasmas, $D_\perp$ is apparently smaller at the LCFS since the slope of the density profile near the separatrix is much steeper in H-modes (by a factor of 2 or more) while the inferred values of S_{main} are similar to those for L-modes (see Fig. 4.3).

Far from the LCFS, the magnitude of the effective $D_\perp$ can greatly exceed the Bohm level (D_{Bohm} is on the order of 0.1 m^2/s in SOL in C-Mod). Such strong growth of $D_\perp$ suggests that the cross-field transport mechanism is not diffusive at these locations. It is more likely that the transport mechanism is convective in nature, perhaps involving a rapid transport of unstable plasma flux tubes towards the wall surfaces.

4.3.2 Midplane neutral density

These observations indicate that the neutral pressure at the main chamber wall is not always a parameter that can be controlled by conventional means such as neutral baffling in the divertor, active pumping in the divertor, or increased LCFS-wall separation distances in the main chamber. Rather, neutral pressures at the outer midplane can be governed more by the cross-field plasma transport in the SOL. The lack of a direct external control of the midplane neutral pressure has important implications for a fusion reactor regarding charge-exchange sputtering of the first-wall, tritium gas inventory, and the auxiliary power needed to achieve the H-mode confinement in presence of high neutral pressure.

4.3.3 Energy transport

Although the SOL particle transport picture is significantly altered by these observations, the energy transport picture is relatively unaffected. Most of the energy flux

coming into SOL from the core is transported to the divertor by the parallel electron heat conduction. For a typical discharge with radial electron temperature profile at the scanning probe location of $T \approx T_{sep} \exp(-\rho/\lambda_T)$, with $\lambda_T \approx 3$ mm, classical electron parallel heat conductivity, $\kappa_{\|} \propto T_e^{5/2}$, poloidal connection length between the probe and the nearest target plate, $\Delta L_c \approx 0.3$ m, major radius R ≈ 0.6 m, and pitch angle $\sin\phi \approx 0.1$, one can estimate the conducted heat as:

$$P_{cond} \approx \frac{2}{7}\kappa_{\|}(T_{sep})\,\frac{T_{sep}}{\Delta L_c}\,(\sin\phi)^2 4\pi R\lambda_T \approx 0.6MW \times \left(\frac{T_{sep}}{50eV}\right)^{3.5} \tag{4.6}$$

For Alcator C-Mod, T_{sep} is typically in the range 40-60 eV, implying that the conducted power is in the range 0.4-1.2 MW, which is consistent with the range of powers entering SOL.

One can also see, using $T \approx 50$ eV and Γ_{div} from Eq. 4.1, that the parallel plasma flow plays almost no role in the transport of thermal energy:

$$P_{conv} \approx \frac{5}{2}T\Gamma_{div}\,\frac{\lambda_T}{\delta\rho} \lesssim 0.1MW \tag{4.7}$$

If the plasma source in the main chamber, S_i, is as high as $10^{23}\ s^{-1}$, then a significant part of energy can be convected rather than conducted across the LCFS. Assuming that the fraction of neutrals penetrating inside the LCFS is $\xi \approx 0.3$, the plasma flux from the core is $\xi S_i \lesssim 0.3 \times 10^{23}\ s^{-1}$. For a separatrix temperature of $T_{sep} \approx 50\ eV$, the convected energy flux from the core can then be estimated as

$$P_{out} \lesssim \frac{5}{2}\xi S_i T_{sep} \approx 0.6MW, \tag{4.8}$$

which can be a significant fraction of total energy flux from the core. This probably explains why there are no H-mode data points in Fig. 4.3 for midplane pressures above some 0.5 mTorr.

4.4 Discussion

In spite of significant uncertainties in the data the principal conclusion that the main chamber recycling fluxes are much larger than the flux into the divertor is quite robust. The Johnson-Hinnov factor, $N_\alpha = 45$, used in Eq. 4.3 for converting the measured D_α brightness into the ionization source, can vary only by a factor of 2 in either way, according to Fig. 4.2. The neutral influx estimate (Eq. 4.4), which should be also correct within a factor of two, is quite consistent with the ionization source estimate (dashed line in Fig. 4.3). Thus the inferred ion source in the main chamber is correct within a factor of 2. On the other hand, the poloidal flux even for a sonic flow ($M \approx 1$) in most cases would be still by a factor of about 3-10 smaller than the inferred core flux. Moreover in many cases the poloidal flux in the SOL is reversed on the outer side [6] which makes the point even stronger.

This idea that main chamber recycling dominates the neutral particle source in the main chamber in C-Mod is consistent with observations of main chamber and divertor gas pressures on C-Mod when a neutral bypass leak in the outer divertor structure was closed: After closure, in L-mode discharges the neutral pressures in the divertor increased by a factor of 2 or more, while the pressures in the main chamber decreased by merely 20% in otherwise identical discharges [6]. This was confirmed in recent C-Mod experiments with a controllable flap plugging the bypass [38]: whether the flapper is open or closed there is no effect on the upstream neutral (and plasma) parameters.

The issue of main chamber recycling has received much attention lately. There are several published reports from different groups where the role of main chamber recycling is discussed.

AUG

The AUG divertor was recently modified to improve neutral gas baffling. However, for a given core density this did not have any effect on the main chamber neutral gas density, a result which was attributed to a significant level of the main chamber recycling [48, 49, 50]. Previously it had been found in numerical modeling of AUG that main chamber recycling is dominant over neutral gas leakage from the divertor in the new divertor configuration [51].

DIII-D

Reports from the DIII-D group strongly advocate the position of divertor recycling and core fueling through the x-point [52]. This seems to be quite different from C-Mod and, apparently, AUG. As DIII-D is quite close to AUG in all major parameters it is puzzling what makes these two machines be so different in this respect.

JET

The JET tokamak has had several different divertor configurations [53]. It was found that in Mark IIAP, a divertor configuration with closed bypass from divertor to main chamber, the midplane neutral gas pressure was lower than in MARK IIA configuration with open bypass [53]. Thus the divertor geometry has a noticeable effect on the main chamber neutral density in JET. This implies that in JET the poloidal particle flux into the divertor is a significant player in the main chamber particle balance which is opposite to what is presently concluded for C-Mod.

JT-60

In investigation of recycling in the JT-60 divertor it was found that a baffle source is needed to match the neutral density inferred from measured D_α emission. This baffle

source was found to be up to 30-40% of the divertor source [54].

Thus dominanance of main chamber recycling is apparently not a universal feature of divertor tokamaks. It is the subject of future work to find what physical processes determine enhanced radial particle transport in the edge plasma. and result in the dominance of main chamber recycling.

4.5 Conclusions

It has been generally assumed that in a tokamak with a divertor, both particles and energy flow from the core into the divertor chamber. In Alcator C-Mod, however, this is apparently not the usual case. Here, plasma out-flux through the SOL, primarily flows to the main chamber walls, while for energy transport, it is probably still true that the energy is transported into the divertor chamber (possibly by the electron heat conduction mechanism). The particle balance in the main chamber is maintained by a back-flux of recycling neutrals from the main chamber walls into the core. In this picture, neutral gas pressure near the walls in the main chamber is determined by the magnitude of the anomalous radial plasma flux rather by baffling of the divertor. The radial profile of plasma density in the SOL implies that the effective plasma diffusion coefficient grows very rapidly across the SOL towards the wall. The energy convected from the core into SOL with the radial flow of plasma can account, in some discharges, for a large fraction, maybe most, of the total energy coming from the core into the SOL.

Chapter 5

Fluid modeling of the edge plasma in C-Mod

As shown in Chapter 4 of this thesis, both the spectroscopic data and mid-plane neutral pressure data indicate that in the main chamber of Alcator C-Mod there exists a significant plasma source (up to $10^{23}s^{-1}$) due to ionization of neutrals. On the other hand Mach probe data indicate that the parallel plasma flow in the SOL of Alcator C-Mod is far too weak to channel such a large flow of ions into the divertor. Thus, in Alcator C-Mod plasmas, a large fraction of the ions flowing out of the core recycle in the main chamber, rather than in the divertor. However, in the traditionally accepted picture of particle transport in the edge plasma in a divertor tokamak [2, 8, 40], all ions flowing out of the core are assumed to be brought to the divertor by the parallel flow in the scrape-off layer (SOL). Thus the processes of plasma recycling and core fueling in the Alcator C-Mod tokamak look very different from that in the traditional picture. To investigate further particle and energy transport in the edge plasma of Alcator C-Mod, the author has conducted numerical modeling of C-Mod [55] with a multi-fluid code UEDGE.

5.1 Fluid model for tokamak edge plasma

5.1.1 Validity of fluid equations for the edge plasma

Without exception, existing two-dimensional plasma edge models are based on fluid equations [56]. Due to its low temperature, the edge region has sufficiently large collisionality to justify application of the fluid equations here. For the fluid approach to be valid, the particle mean free path λ must be small compared with any characteristic along-field scale length, $L_{\|}$. For the cross-field direction, the validity condition is that the particle gyroradius, r_L, be small compared with any characteristic cross-field length $L_{\perp}$.

The mean free path for both thermal electrons and ions can be estimated as

$$\lambda \approx 1.5 \cdot 10^{12} \frac{T^2}{n} \; [cm] \tag{5.1}$$

where T is the plasma temperature in eV, n is the plasma density in cm^{-3}.

The gyroradius is

$$r_L \approx 100 \frac{T^{1/2}}{B} \; [cm] \tag{5.2}$$

where T is in eV and B in Gauss.

For C-Mod the typical parameters in the edge plasma are $T \sim 50$ ev, $n_e \sim 10^{14}\ cm^{-3}$, B $\sim 5 \times 10^4$ Gauss, and typical scale lengths are $L_{\|} \sim 10\ m$ and $L_{\perp} \sim 3\ mm$. With these parameters one finds, using Eq. 5.1 and 5.2, $\lambda \sim 30$ cm and $r_L \sim 0.1$ mm. One can see that $\lambda \ll L_{\|}$ and $r_L \ll L_{\perp}$, and thus the fluid equations should be valid here. One should note that the electron heat conduction is dominated by electrons from the high energy tail of the distribution for which the mean free path may be an order of magnitude larger than that given by Eq. 5.1. Still, the fluid equations should be applicable, except for the vicinity of the target plates where the parallel gradients

are steep and $\lambda \gtrsim L_{||}$. At the target plates, the fluid equations are closed using a boundary condition that simulates the collisionless sheath region.

5.1.2 Description of the UEDGE model

The UEDGE code is one of the most elaborate presently existing edge codes. It was originally developed by Rognlien et al. [57]. This is a 2-D multifluid code. The equations solved in UEDGE are based on the reduced Braginskii equations [56] which are solved in the curvilinear magnetic coordinates (see Appendices A and B for details). Additional assumptions used in the formulation of the equations being solved in our version of the code are

- Toroidal symmetry
- Plasma is quasineutral, the flow is ambipolar $\Rightarrow \vec{j} = 0$, no separate electron momentum.
- Cross-field drift terms are neglected.
- Ion velocity in diamagnetic direction is neglected $\Rightarrow$ one component in the ion momentum equation is eliminated.
- Anomalous radial transport is assumed to be much stronger than the classical terms $\Rightarrow$ radial diffusion equations, no classical terms for radial fluxes.
- One temperature is assumed for all ions and neutrals.
- Viscosity tensor is simplified $\Rightarrow$ cross-field derivative terms neglected.

The parallel transport is treated classically as prescribed by Braginskii, that is as for weakly non-Maxwellian plasma, whereas the radial transport is assumed to be anomalous, described by empirical diffusion coefficients (and possible pinch velocities).

With all these assumptions, the UEDGE equations are as follows [58, 57, 59] (x is the poloidal coordinate, y the radial coordinate).

The continuity equation for ions:

$$\frac{\partial n_i}{\partial t} + \frac{\partial (n_i V_{ix})}{\partial x} + \frac{\partial (n_i V_{iy})}{\partial y} = (K_i - K_r) n_e n_n \tag{5.3}$$

where the source term is given by ionization and recombination; $K_i =< \sigma_i v_e >$ and $K_r =< \sigma_r v_e >$ are the rates of ionization and recombination respectively.

Summing the electron and ion momentum equations and taking the parallel component one finds the equation for the parallel plasma velocity:

$$\begin{aligned} &\frac{\partial}{\partial t}(n_i m_i V_{i\|}) + \frac{\partial}{\partial x}(n_i m_i V_{ix} V_{i\|} - \eta_x \frac{\partial V_{i\|}}{\partial x}) + \frac{\partial}{\partial y}(n_i m_i V_{iy} V_{i\|} - \eta_{ay} \frac{\partial V_{i\|}}{\partial y}) + \\ &\frac{B_x}{B}\frac{\partial}{\partial x}(p_i + p_e) = m_i n_i n_n K_{cx}(V_{i\|} - V_{n\|}) - m_i n_e (n_i K_r V_{i\|} - n_n K_i V_{n\|}) \end{aligned} \tag{5.4}$$

where the source term describes momentum exchange with the neutrals through ionization, recombination and charge-exchange, K_{cx} being the charge exchange rate. The cross-field viscosity η_{ay} is anomalous.

The poloidal plasma velocity V_{ix} is given by

$$V_{ix} = \frac{B_x}{B} V_{i\|} \tag{5.5}$$

The radial plasma velocity V_{iy} is given by

$$V_{ix} = -\frac{D_a}{n_i}\frac{\partial n_i}{\partial y} + V_a \tag{5.6}$$

where D_a is the anomalous plasma diffusion coefficient, V_a is the pinch velocity.

The electron internal energy equation is

$$\frac{\partial}{\partial t}(\frac{3}{2}n_eT_e) + \frac{\partial}{\partial x}(\frac{5}{2}n_eT_eV_{ex} - k_{ex}\frac{\partial T_e}{\partial x}) + \frac{\partial}{\partial y}(\frac{5}{2}n_eT_eV_{ey} - k_{ey}\frac{\partial T_e}{\partial y}) = \tag{5.7}$$
$$V_{ex}\frac{\partial p_e}{\partial x} + V_{ey}\frac{\partial p_e}{\partial y} - K_q(T_e - T_i) + S_{E.e}$$

where $K_q(T_e - T_i)$ is rate of energy exchange between ions and electrons, ($K_q = (3m_e/m_i)n_e/\tau_e$). The electron energy loss by radiation is given by the S_{E_e} term. Also, $V_{ex} = V_{ix}$, $V_{ey} = V_{iy}$.

The internal energy equation for ions+neutrals is (j denotes ion species):

$$\Sigma_j[\frac{\partial}{\partial t}(\frac{3}{2}n_jT_i) + \frac{\partial}{\partial x}(\frac{5}{2}n_jT_iV_{jx} - k_{jx}\frac{\partial T_i}{\partial x}) + \frac{\partial}{\partial y}(\frac{5}{2}n_jT_iV_{jy} - k_{jy}\frac{\partial T_i}{\partial y}) = \tag{5.8}$$
$$V_{jx}\frac{\partial p_j}{\partial x} + V_{jy}\frac{\partial p_j}{\partial y} + \eta_{jx}(\frac{\partial V_{j\|}}{\partial x})^2 + \eta_{jy}(\frac{\partial V_{j\|}}{\partial y})^2 + K_q(T_e - T_i) +$$
$$\frac{1}{2}m_jV_{i\|}^2n_j\nu_{jz} + S_{E,j}] + \frac{1}{2}m_h(V_{hi\|} - V_{hn\|})^2(2n_{hi}n_{hn}K_{cx} + n_en_{hn}K_i + n_en_{hi}K_r)$$

where h stands for the hydrogenic species.

The neutral continuity equation:

$$\frac{\partial n_n}{\partial t} + \frac{\partial(n_nV_{nx})}{\partial x} + \frac{\partial(n_nV_{ny})}{\partial y} = -(K_n - K_r)n_en_n \tag{5.9}$$

The equation for the parallel neutral velocity:

$$\frac{\partial}{\partial t}(n_nm_iV_{n\|}) + \frac{\partial}{\partial x}(n_nm_iV_{nx}V_{n\|} - \eta_{nx}\frac{\partial V_{n\|}}{\partial x}) + \frac{\partial}{\partial y}(n_nm_iV_{ny}V_{n\|} - \eta_{ny}\frac{\partial V_{n\|}}{\partial y}) + \tag{5.10}$$
$$\frac{B_x}{B}\frac{\partial p_n}{\partial x} = m_in_in_nK_{cx}(V_{i\|} + V_{n\|}) + m_in_e(n_iK_rV_{i\|} - n_nK_iV_{n\|})$$

where the neutral viscosity is of the form

$$\eta_{ny} = \frac{C_1 T_i}{m K_{cx}} \frac{n_n}{n_i + C_2 n_n} \tag{5.11}$$

with C_1, C_2 some constants of the order of unity.

The perpendicular neutral velocity is diffusive

$$V_{\perp n} = -\frac{\nabla_\perp (n_n T_n)}{m_i n_n n_i K_{cx}} \tag{5.12}$$

The above fluid equations are closed by appropriate boudary conditions at the material wall and at the core plasma interface. Options for this are described in detail in the UEDGE user manual [59]. For the case of a single ion species, the code solves for six main variables: n_i, n_n, T_i, T_e, $V_{n\|}$, $V_{i\|}$.

5.1.3 Computational aspects

The fluid equations described in the previous section describe the time evolution of the unknowns. They form a system of highly non-linear differential equations. The standard approach to solving such systems is discretization on a computational mesh, linearization and solving iteratively the linearized system.

The equations, discretized on the mesh, can be written compactly as

$$\frac{\partial \vec{f}}{\partial t} = \vec{F}(\vec{f}) \tag{5.13}$$

The vector of unknowns $\vec{f}$ represents all unknown variables at all locations on the computational mesh.

The time derivative on the left-hand side is approximated by a finite difference and in the right hand side a predicted value of $\vec{f}$ is used (or a some kind of a weighted average). Then the equations become, for the j^{th} time step,

$$(\vec{f}_{j+1} - \vec{f}_j)/\delta t = \vec{F}(\vec{f}_{j+1}) \tag{5.14}$$

The initial state vector $\vec{f}_j$ is known, which makes Eq. 5.14 a system of non-linear transcendental equations that must be solved for the predicted state vector $\vec{f}_{j+1}$. This is done by Newton iteration [29] by solving a sequence of linearized problems. However the enormous size of the system (six equations times a few hundred or more mesh nodes) and high non-linearity of the equations makes this a challenging task. The state-of-the-art linear solvers developed by UEDGE creators use special methods such as matrix preconditioning, Newton-Krylov method etc. for solving these large linear systems. Still, there is no guarantee that the iterations will converge, unless the time step δt is taken sufficiently small, which makes the off-diagonal elements of the resulting matrix small, so that the matrix can more easily be inverted.
Usually, a steady-state solution is sought which may be found by following the time evolution to infinity. Other options are described in detail in the UEDGE user manual [59].

5.2 Analysis of C-Mod with UEDGE

5.2.1 Geometry

The modeling presented here is focused primarily on the transport behavior in the scrape-off layer. The modeling is done using an orthogonal mesh geometry which is beneficial for the code convergence properties. It is realized that such a simplified geometry does not describe properly the divertor but for the main SOL well above the divertor, it is acceptable. A locally orthogonal computational mesh covers a domain representing the edge plasma of C-Mod as shown in Fig. 5.1. The dashed line defines the boundary between the main chamber and the divertor chamber. Particle flux into

the divertor, Γ_d, is integrated between points A and B.

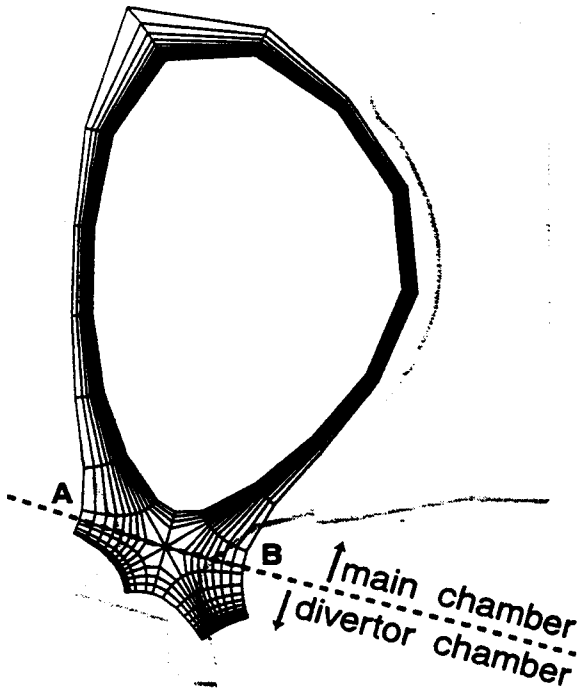

Figure 5.1: Computational mesh used in the modeling is shown with the contour of the actual wall of C-Mod in the poloidal plane.

5.2.2 Boundary conditions

In a steady state, the plasma particle flux from the core (throughput) can be sustained by an ionization source in the main plasma balanced by particle pumping at the wall. Plasma sources in the core can indeed exist in a tokamak due to pellet injection or neutral beam injection. However, in Alcator C-Mod, a steady state is achieved

without any externally supplied particle sources in the main plasma. A detailed analysis [37] showed that both the gas injection and the wall pumping rates in C-Mod are small compared to the recycling fluxes. This allows us to estimate a lower bound on the recycling coefficient R. In C-Mod the core plasma density is $\bar{n} \approx 10^{20}\ m^{-3}$ and the core plasma volume $V_{core} \approx 1\ m^3$, hence the total particle content in the core plasma in C-Mod is $N_{core} \sim \bar{n} V_{core} \sim 10^{20}$. Since the core plasma density does not decay on time scale $\tau \sim 1$ s the net particle flux from the core does not exceed $\Gamma_{core} \sim N_{core}/\tau \sim 10^{20}\ s^{-1}$. This is very small ($\lesssim 0.1\%$) compared to the recycling fluxes which are of the order of $10^{23}\ s^{-1}$ in C-Mod. Thus one can conclude that in C-Mod the recycling coefficient of the wall surfaces is very close to unity ($\gtrsim 0.999$) otherwise plasma would not exist that long.

Due to this argument gas injection is not included in this modeling and the whole external boundary of the computational domain including the divertor plates and the side wall is modeled as a fully recycling material wall. The latter implies coupling of the radial particle fluxes for ions and neutrals at the wall $\Gamma_{iy} = -\Gamma_{ny}$, and also coupling of the radial heat flux at the wall with local plasma and neutral densities and temperatures $q = \delta_e T_e j_{ey} + \delta_i T_i j_{iy} + \delta_N n_N C_s(T_{iN}) T_{iN}$ where each of the terms describes electron, ion and neutral contributions, δ are the sheath transmission coefficients, and C_s is the sound speed. At the divertor plates, the parallel velocity is set to be sonic and at the side wall the plasma density is set according to probe measurements in the far SOL. This completes the set of boundary conditions for the plasma density, neutral density, and energy equations at the plates and the side wall.

At the inner boundary of the computational domain (the core interface) the input power and plasma density are specified, providing the boundary conditions for the plasma energy and density equations. The boundary condition for the neutral density equation at the core interface is provided by setting the neutral particle flux density to zero, since the neutral ionization mean free path is comparable to the SOL width and

most of neutrals are ionized outside of the core interface. The modeling results did not change significantly when the innermost flux surface was moved further in. Note that the described set of boundary conditions automatically provides zero plasma particle throughput in steady state.

5.2.3 Modeling of radial profiles of plasma density and temperature in scrape-off layer

In the present modeling it is found that it is impossible to match the experimental radial profile of plasma density in the SOL using a spatially uniform anomalous plasma diffusion coefficient $D_\perp$. As an illustrative case, the author solved for 2-D plasma density profiles using UEDGE with various values of spatially constant anomalous plasma diffusion coefficient $D_\perp$. In all cases, the cross-field plasma density profile in the SOL appears to have the wrong curvature for various values of $D_\perp$ as shown in Fig. 5.2.

The main cause of this curvature mismatch is the large ionization source in the SOL due to high neutral density there. Matching the plasma density profiles in the SOL turns out to be possible by using a plasma diffusion coefficient which grows radially towards the wall.

In the present work, two C-Mod discharges were modeled: shot 950607021 with core plasma density $\bar{n}_e \approx 2.4 \times 10^{20}\ m^{-3}$ and relatively high mid-plane gas pressure, $P_{mid} \approx$ 0.3 mTorr, and shot 960208031 with core plasma density $\bar{n}_e \approx 1.2 \times 10^{20}\ m^{-3}$ and low $P_{mid} \approx 0.025$ mTorr. Both shots are Ohmic L-modes with parameters typical for C-Mod operations: plasma current $I_p \approx 0.8$ MA and the power flow across the separatrix into the SOL $P_{sol} \approx 0.7$ MW. For both shots the SOL profiles of plasma density and temperature look quite typical for C-Mod.

In the modeling, the input power P_{sol} was set close (within 25%) to the experimentally

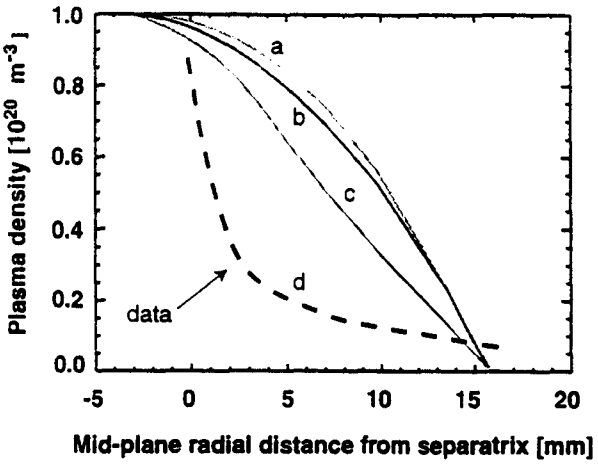

Figure 5.2: Calculated radial profiles of plasma density for spatially constant anomalous diffusion coefficient: (a) $D_\perp = 0.5\ m^2/s$, (b) $D_\perp = 0.1\ m^2/s$, (c) $D_\perp = 0.02\ m^2/s$. For all presented cases the anomalous heat diffusivity $\chi_\perp$ was set $0.25\ m^2/s$. A typical experimental profile is shown by dashed line (d).

inferred value. The anomalous plasma diffusion coefficient $D_\perp(\rho)$ as a function of the flux surface, and the anomalous plasma heat diffusivity $\chi_\perp$ ($\chi_{\perp i} = \chi_{\perp e} = \chi_\perp$) for plasma were adjusted to match the calculated profiles of electron density and temperature in the SOL to those measured by a fast-scanning probe (FSP) [6].

A spatially constant plasma heat diffusivity, $\chi_\perp$, sufficed to achieve a reasonably good match with the experimental electron temperature profiles. The value of $\chi_\perp$ is 0.1 m^2/s for the high P_{mid} case and 0.5 m^2/s for the low P_{mid} case. This is consistent with the results of $\chi_\perp$ analysis in Chapter 3, both in the magnitude of $\chi_\perp$ and in the conclusion that spatially uniform $\chi_\perp$ describes well the data.

The results showing the matches to the experimental plasma density and temperature profiles are shown in Fig. 5.3 and Fig. 5.4. A good match with the experimental SOL

density profiles could also be achieved by using a spatially uniform $D_\perp$ of the order of 1 m^2/s combined with a spatially uniform radial inward pinch of the order of a few tens m/s, or without any diffusive term by using an outward radial "anti-pinch" growing in magnitude towards the wall.

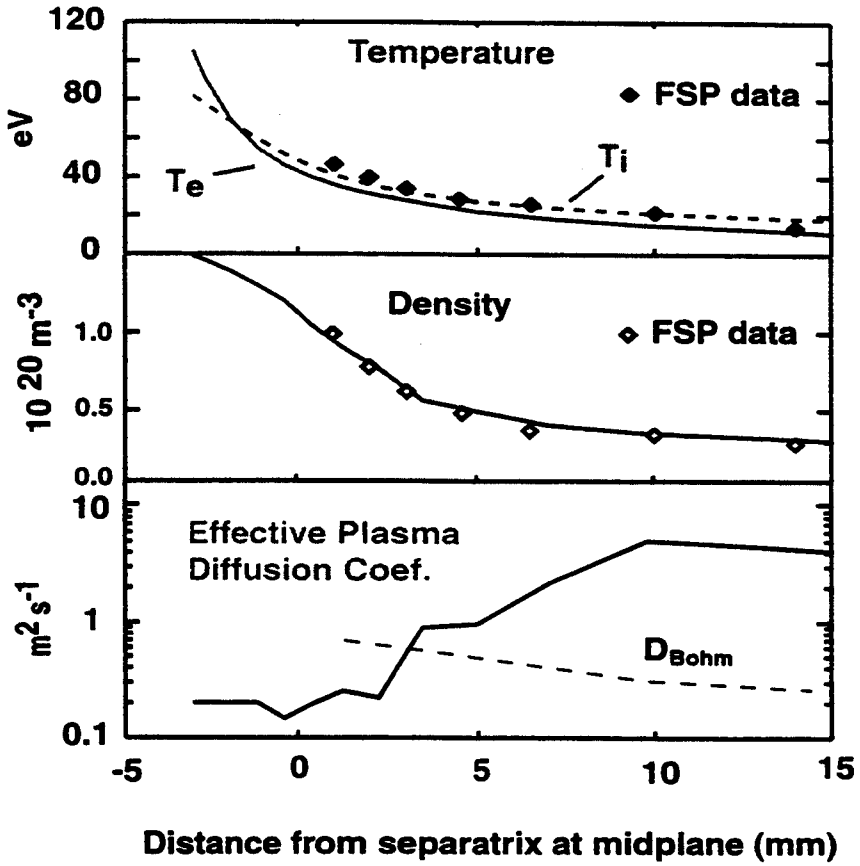

Figure 5.3: High P_{mid} case. Calculated radial profiles of n_e and T_e at the outer mid-plane are fitted to the data by using non-uniform effective plasma diffusion coefficient. The anomalous heat diffusivity is uniform (0.1 m^2/s).

For both shots the mid-plane gas pressure was matched within 25%. The mid-plane pressure, P_{mid}, in these calculations was inferred from the neutral temperature and

density at the wall assuming kinetic flux balance between the molecules in the pressure gauge and the atoms near the wall.

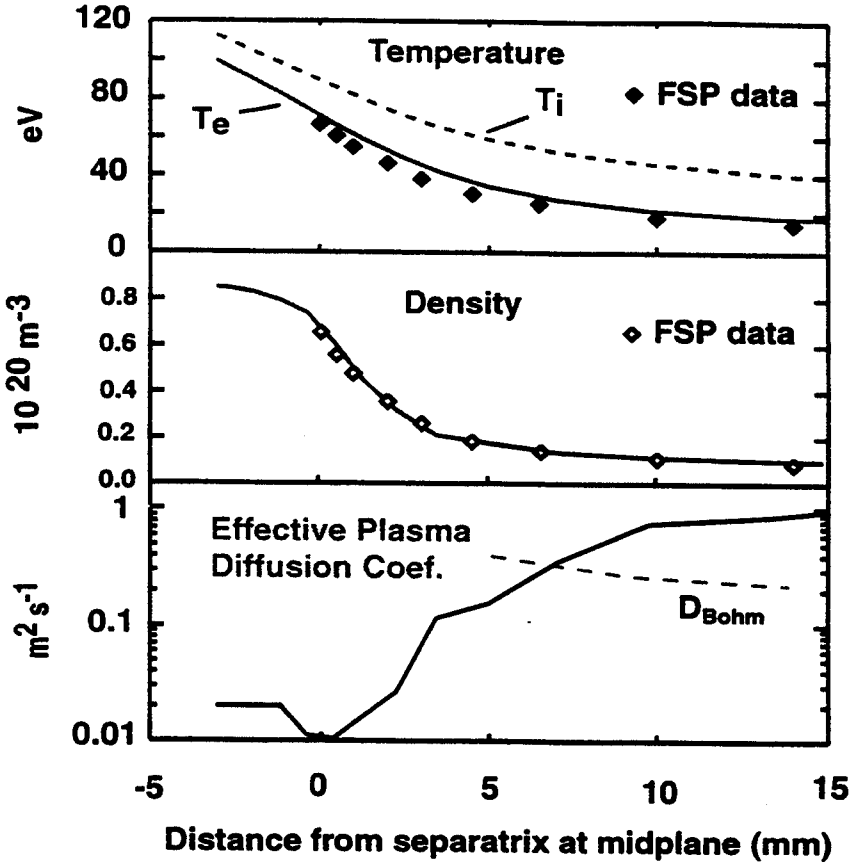

Figure 5.4: Low P_{mid} case. Calculated radial profiles of n_e and T_e at the outer mid-plane are fitted to the data by using non-uniform effective plasma diffusion coefficient. The anomalous heat diffusivity is uniform (0.5 m^2/s).

For both modeled discharges the chord-integrated D_α brightness for a horizontal view through the mid-plane of the plasma turned out to be smaller than the experimental value by a factor of about 3. The author has not, as yet, been able to determine the primary cause of this discrepancy. Most likely it is largely due to fluid treatment of

neutrals instead of a true kinetic treatment which would be more appropriate here since the mean free path for the neutrals is comparable to the width of the SOL. Indeed, the depth of neutral penetration into the plasma in the diffusive model can be estimated as $\sqrt{\lambda_{cx}\lambda_{ion}}$ from the random walk arguments. Here λ_{ion}, λ_{cx} are mean free path lengths due to CX scattering and ionization processes. Diffusive model implies that many CX scattering events occur before ionization. However if the neutral particle can do just a few random steps before ionization, the penetration depth is on the order of λ_{ion}. Thus the diffusive model tends to over-estimate the penetrations depth and the plasma density at which radiation and ionization occur. This, according to Fig. 4.2, results in fewer photons emitted per an ionization event. Another possible cause is that interpretation of the pressure gauge data using the simple kinetic balance arguments may be not quite accurate due to the complicated geometry of the gauge. Reflections of light from the walls of the vessel can also amplify slightly (by some 20-30%) the measured D_α brightness.

5.2.4 Particle flux balance and core fueling

To analyze transport of particles in the edge plasma it is convenient to consider separately the "main SOL" domain and the "X-point SOL" domain, which are defined as shown in Fig. 5.5.

The main SOL is the part of the SOL above the level of the scanning probe which makes this definition convenient for benchmarking of the modeling against the probe data. The X-point SOL is the lower part of the SOL. The "whole SOL" domain is the union of the main SOL and the X-point SOL. The lower poloidal edge of each domain is defined as its "bottom". For the main SOL, the bottom is the boundary between the main SOL and the X-point SOL. For both the X-point SOL and the whole SOL, the bottom is the boundary between the main chamber and the divertor

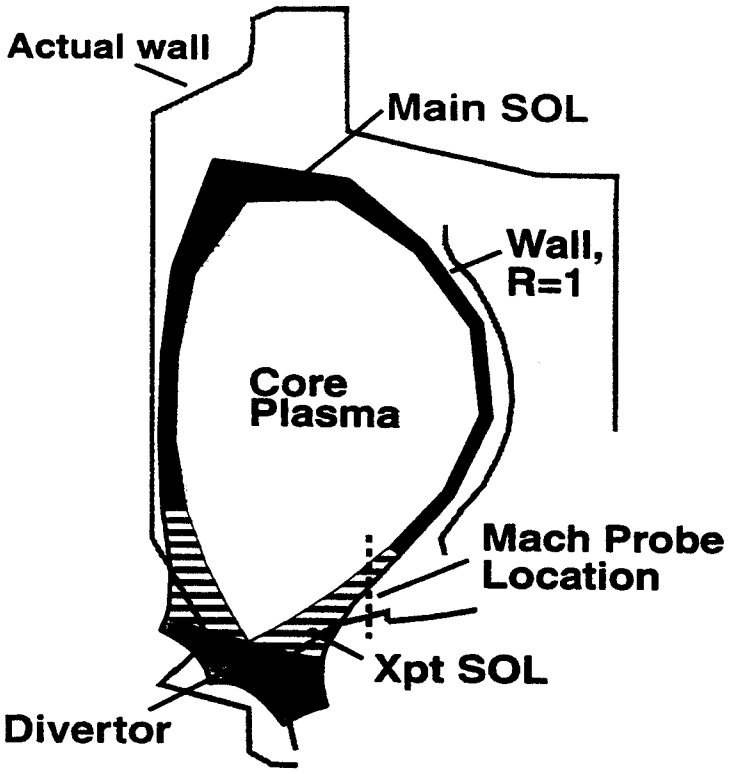

Figure 5.5: The main SOL domain is defined as the part of the SOL lying above the Mach probe location. The main SOL domain has three types of boundaries: outer wall, separatrix and the bottom which is defined as the lower edge of the main SOL domain.

chamber. For each of the three domains (main SOL, X-point SOL and the whole SOL) we consider the total poloidal particle flux through the bottom, Γ_{bot}, and radial particle fluxes through the outer wall boundary, Γ_{wall}, and through the separatrix, Γ_{sepx}. Approximate values of these fluxes for ions and neutrals are presented in Tables 5.1 and 5.2 for the low P_{mid} and the high P_{mid} cases respectively. Flux directions are assumed to be positive for Γ_{wall} directed towards the outer wall, for Γ_{sepx} directed out of the core and for Γ_{bot} directed towards the divertor.

First, analyzing the particle balance for the whole SOL domain using Tables 5.1 and

5.2, one can see that in both cases the total flux of ions escaping to the wall and into the divertor, $\Gamma_{wall} + \Gamma_{bot}$, is much larger than the ion flux entering the SOL from the core, Γ_{sepx}. This means that neutral fueling of the SOL is much larger than neutral fueling of the core. The fraction of the ionization source above the X-point level which is located inside the last closed flux surface (LCFS) is given by the ratio $\Gamma_{sepx}/(\Gamma_{wall} + \Gamma_{bot})$. According to Tables 5.1 and 5.2 this fraction is about 0.2 for both the high P_{mid} and the low P_{mid} cases.

Part of	Γ_{wall} $[s^{-1}]$		Γ_{sepx} $[s^{-1}]$		Γ_{bot} $[s^{-1}]$	
SOL	ion	neutral	ion	neutral	ion	neutral
Main	7.9×10^{20}	-7.9×10^{20}	6.9×10^{20}	-3.3×10^{20}	4.2×10^{20}	-6.7×10^{19}
X-pt	6.9×10^{19}	-6.9×10^{19}	1.9×10^{20}	-5.4×10^{20}	2.6×10^{21}	-2.6×10^{21}
Whole	8.6×10^{20}	-8.6×10^{20}	8.7×10^{20}	-8.7×10^{20}	2.6×10^{21}	-2.6×10^{21}

Table 5.1: Particle flux balance in the low P_{mid} case. For the whole SOL draining by the poloidal flux is larger by a factor of ~ 3 than the flux to the wall. However for the main SOL the flux to the wall is larger by a factor of ~ 2 than the poloidal flux and thus the main SOL is dominated by wall recycling.

Part of	Γ_{wall} $[s^{-1}]$		Γ_{sepx} $[s^{-1}]$		Γ_{bot} $[s^{-1}]$	
SOL	ion	neutral	ion	neutral	ion	neutral
Main	2.7×10^{22}	-2.7×10^{22}	1.1×10^{22}	-5.4×10^{21}	6.3×10^{21}	-1.0×10^{21}
X-pt	1.6×10^{22}	-1.6×10^{22}	2.9×10^{21}	-8.2×10^{21}	1.9×10^{22}	-1.9×10^{22}
Whole	4.2×10^{22}	-4.2×10^{22}	1.4×10^{22}	-1.4×10^{22}	1.9×10^{22}	-1.9×10^{22}

Table 5.2: Particle flux balance in the high P_{mid} case. The poloidal flux at the bottom of the whole SOL is smaller by a factor of ~ 2 than the flux to the wall. Here main wall recycling dominates particle balance for the whole SOL.

Next, we compare the magnitudes of Γ_{wall} and Γ_{bot} for the whole SOL. In the low P_{mid}

case, Γ_{bot} is larger than Γ_{wall} by a factor of about 3, which means that the ionization source in the main chamber is primarily balanced by the poloidal ion flux into the divertor. However, in the high P_{mid} case, Γ_{wall} is greater than Γ_{bot} by a factor of about 2, and thus recycling of plasma on the main wall becomes an important player in the particle balance. Note that in some C-Mod discharges the magnitude of P_{mid} can reach values as high as a few mTorr. It seems likely that for such extremely high P_{mid} cases recycling of plasma on the main wall completely dominates the particle balance in the SOL.

Examining the particle fluxes in Tables 5.1 and 5.2 for the main SOL, one can see that in both the high P_{mid} and low P_{mid} cases, the ion and neutral particle fluxes through the bottom of the main SOL cannot balance particle fluxes flowing in the radial direction. A large ion flux to the outer wall is sustained by a significant ionization source in the main SOL. Thus in the main SOL the particle balance is predominantly radial, even in the low P_{mid} case.

The poloidal ion flux through the divertor throat, Γ_{bot} for the whole SOL, is much larger than Γ_{bot} for the main SOL. This is because of a large ionization source in the X-point SOL domain. As can be seen from Table 5.2, in the high P_{mid} case, the lower part of the main wall takes a large fraction of the wall particle flux.

It is important that the parallel flow appears to be a secondary effect for the particle balance in the main SOL. The calculated poloidal ion flux through the bottom of the main SOL can be compared with experiment, since both plasma density and parallel velocity data are available from the Mach probe. Typically, the parallel velocity of plasma flow in the SOL is 1-10 km/s in C-Mod, according to the probe measurements [6]. In the present modeling it is found that the parallel velocity near the probe's location has the right order of magnitude. Since the density profiles in the SOL are matched quite accurately, the calculated poloidal ion flux at the bottom of the main SOL should also have the right order of magnitude.

The poloidal distribution of particle flux density across the LCFS is shown in Fig. 5.6.

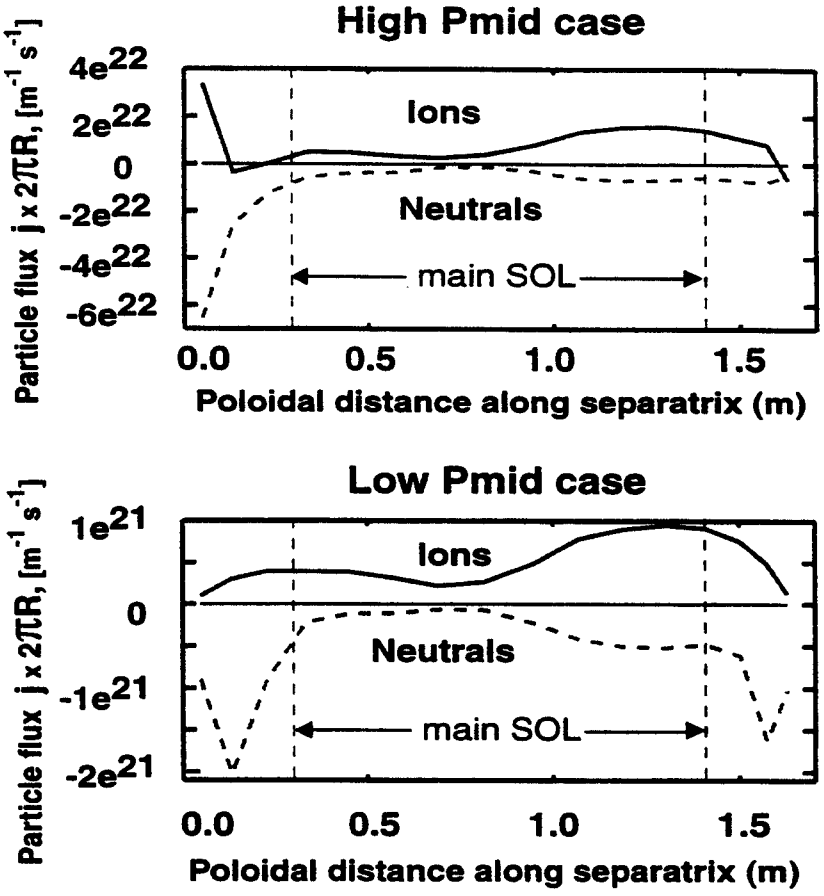

Figure 5.6: Radial particle flux density across LCFS, j, scaled by $2\pi R$, where R is the local major radius, plotted against the length of the poloidal projection of the separatrix clockwise from x-point to x-point. The end points on the x-axis correspond to the x-point. The vertical dashed lines correspond to the boundaries of the main SOL domain. Outward flux has positive sign.

The radial particle flux density at the separatrix, scaled by a factor $2\pi R$ (evaluated locally), is plotted as a function of the poloidal distance along separatrix. The x-coordinate starts from the X-point and follows clockwise along the separatrix coming

back to the X-point. One can see in Fig. 5.6 that the contribution to the radial ion flux is larger at the outer side. This is mainly because, at the outer side, the compression of magnetic surfaces is larger. Fig. 5.6 and Tables 5.1 and 5.2 demonstrate that the core plasma is mostly fueled by neutrals penetrating through the lower part of the LCFS.

In the modeling for the low P_{mid} case, it was found that poloidal plasma flow at the separatrix is directed out of the divertor in both the inner and the outer SOL regions. A reverse flow at the separatrix is often seen in C-Mod experiments in the outer SOL [6] but no data is available for the inner side. One should note that in C-Mod the parallel flow in the SOL, and the reverse flow in particular, depends on the direction of the toroidal magnetic field, which is apparently related to the plasma drifts [60]. This feature cannot be examined in the present modeling, since drifts are not included here.

5.2.5 Radial heat transport

The radial heat flux in the model is given by

$$q_{tot} = q_{anom} + q_{ecnv} + q_{incnv} + q_{cx} \tag{5.15}$$

where q_{anom} is the flux due to the anomalous radial heat conduction by plasma, q_{ecnv} is the radial heat flux convected by electrons, q_{incnv} is the radial heat flux convected by ions and neutrals and q_{cx} is the heat flux conducted by the neutrals.

The anomalous heat flux conducted by the plasma is

$$q_{anom} = -n_e \chi_\perp \nabla_\perp T_e - n_i \chi_\perp \nabla_\perp T_i \tag{5.16}$$

where n_e and n_i are densities of electrons and ions, T_e and T_i are the temperatures, and $\chi_\perp$ is the anomalous heat diffusivity.

The heat flux conducted by neutrals is given by

$$q_{cx} = -\kappa_{cx} \nabla_{\perp} T_i \tag{5.17}$$

where κ_{cx} is the heat conductivity associated with the presence of neutrals in plasma (mainly due to the charge-exchange processes)

$$\kappa_{cx} \approx n_n \lambda_{cx}^2 \nu_{cx} \approx \frac{n_n}{n_i \sigma_{cx}} V_{tn} \tag{5.18}$$

where V_{tn} is the neutral thermal velocity, n_n the neutral density, λ_{cx} is the mean free path for charge-exchange, and ν_{cx} is the frequency of charge-exchange.

The radial heat flux convected by electrons is

$$q_{ecnv} = \frac{5}{2} T_e j_{rp} \tag{5.19}$$

and the radial heat flux convected by ions and neutrals is

$$q_{incnv} = \frac{5}{2} (T_i j_{rp} + T_n j_{rn}) \tag{5.20}$$

where T_n is the neutral temperature, j_{rp} is the radial plasma particle flux density, and j_{rn} is the radial neutral flux density. In some cases q_{incnv} may become negative due to a slight imbalance between ion and neutral radial particle fluxes at a particular flux surface.

In Fig. 5.7 the total radial power flux across the SOL and all its components (integrated over the flux surface above the x-point level) are plotted against the radial coordinate ρ, the distance from the separatrix at the mid-plane.

One can see that, in the high P_{mid} case, heat convection by plasma and heat conduction by CX neutrals dominate the heat transport across the whole SOL. In the high P_{mid} case, these two power channels account for $\sim 75\%$ of P_{sol}, the total power coming

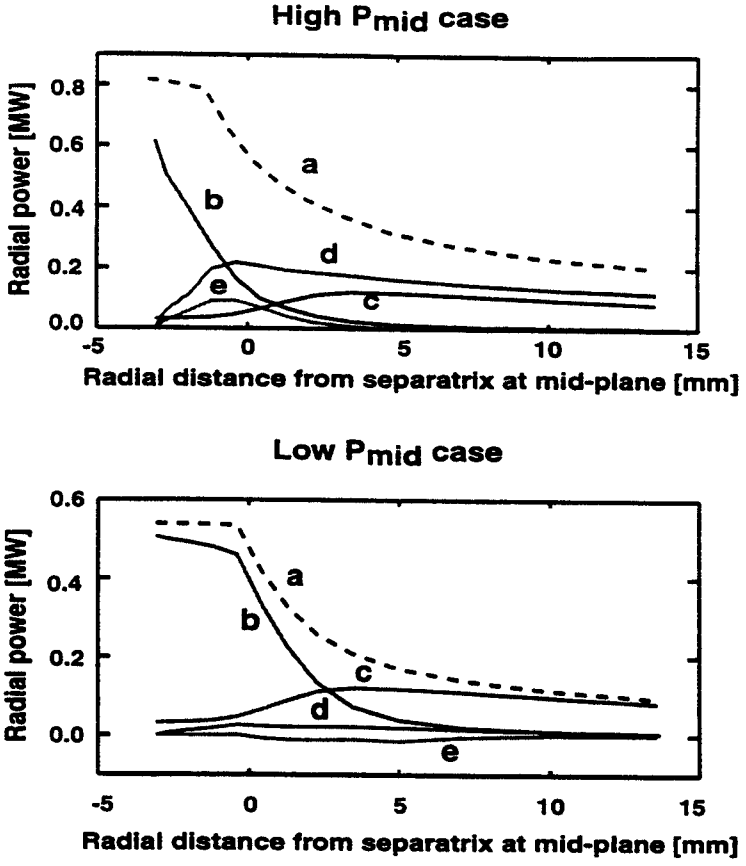

Figure 5.7: Radial heat flux in SOL: total (a), anomalous conduction (b), conduction by CX neutrals (c), convection by electrons (d), convection by ions and neutrals (e).

from the core. In the low P_{mid} case heat convection is small, while heat conduction by CX neutrals dominates the radial heat flux for $\rho \gtrsim 3\ mm$. In the low P_{mid} case, the neutral density near the wall is about a factor of 10 smaller than in the high P_{mid} case. However, the effect of heat conduction by CX neutrals is still quite significant in the low P_{mid} case, since the plasma density in the SOL is roughly proportional to P_{mid}, which makes κ_{cx} vary only slightly.

5.2.6 Discussion

Two features of the anomalous particle transport, represented by an effective diffusion coefficient $D_\perp$, are evident from the present modeling. First, the profiles of $D_\perp$ are very similar in both the low P_{mid} and the high P_{mid} cases, with the effective $D_\perp$ growing rapidly across SOL. This suggests that a mechanism different from diffusion governs the anomalous particle transport in the SOL [42]. Second, the magnitude of $D_\perp$ is much larger in the high P_{mid} case. The data presented in Fig. 5.8 show that the mid-plane pressure P_{mid} increases roughly as cube of the core plasma density, $\bar{n}_e$, in L-modes. Thus the plasma transport from the core also grows quite rapidly with the core density.

Empirical scaling of P_{mid} vs. the core plasma density, n_{core}, is shown in Fig. 5.8 where data from about 500 shots are presented.

In L-modes the mid-plane gas pressure grows approximately as the core plasma density cubed which implies that the anomalous transport of plasma from the core grows rapidly with the core plasma density. The dashed line shows the best linear fit to the L-mode data. All shown discharges have a single X-point configuration with most of them having the X-point at the bottom. The data presented in Fig. 5.8 show that the mid-plane gas pressure, P_{mid}, scales with the core density quite differently in L-modes than in H-modes. This suggests that P_{mid} is related to intrinsic properties of the plasma and in particular the anomalous particle transport.

As shown in Fig. 5.8 for given core plasma density in L-mode discharges the mid-plane gas pressure is about the same no matter whether the X-point is at the top or at the bottom of the machine. The target plate geometry is very different in these two cases (see Fig. 5.1). This indicates that the target plate geometry is not important for transport in the main SOL, which justifies the simplified orthogonal geometry used in this modeling.

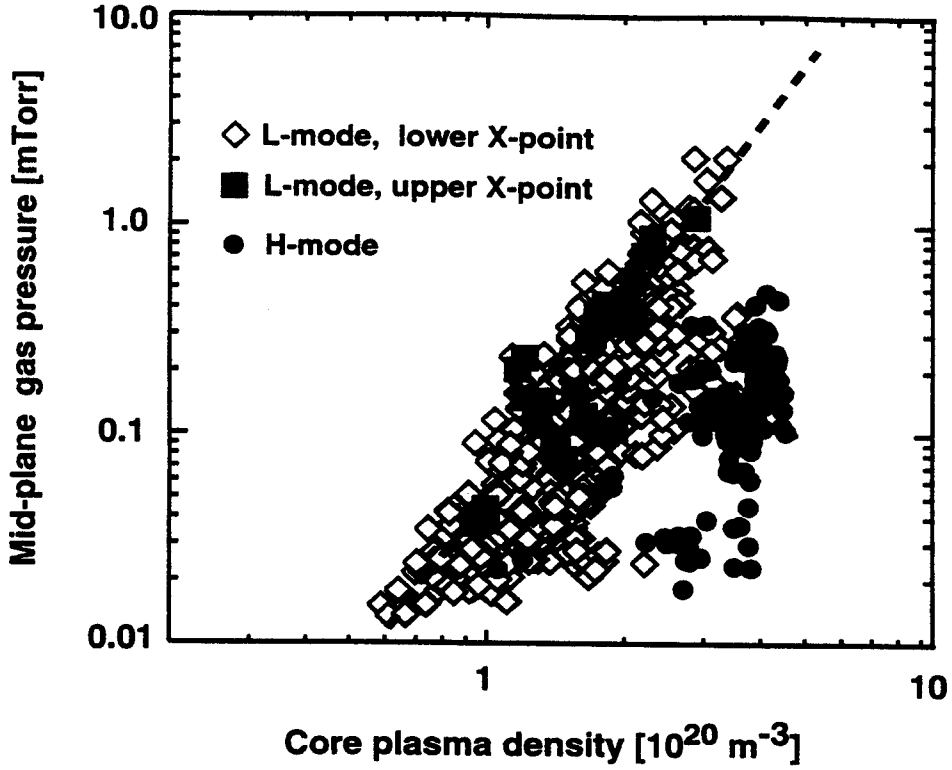

Figure 5.8: Empirical scaling of P_{mid} vs. the plasma density n_{core}.

Besides the problem with simplified geometry there is a problem with fluid treatment of neutrals in these calculations, as the fluid treatment is only marginally valid here. In an attempt to make a correction for kinetic effects one can use a flux-limiting factor for κ_{cx}

$$\kappa_{cx}^{fl} = \frac{\kappa_{cx}}{1 + |C\frac{\lambda_{cx}}{\lambda_T}|} \tag{5.21}$$

where λ_T is the characteristic scale of radial temperature variation and C is a constant of order of unity. However comparing calculations done with and without such a flux-limiting factor, it was found that all results are quite similar, which lends more confidence in the results presented here.

However, as the diffusive model for radial neutral transport used in the code is less reliable for very steep edge profiles of density and temperature which occur in H-modes, modeling of H-mode discharges was not conducted in the present work.

It is not clear yet whether the picture of particle transport and core fueling in other tokamaks is similar to what is found here for C-Mod. Note that C-Mod occupies a unique position among other tokamaks due to its molybdenum walls, high core density, high magnetic field and compact size. It is possible that the anomalous transport across the LCFS in C-Mod is higher than in other machines.

It has been long known that high mid-plane neutral pressure is associated with degradation of confinement in C-Mod [61] and other tokamaks [62, 63, 64]. and it has been speculated that better baffling of the neutral gas in the divertor can lead to improved confinement. However the present results suggest that in C-Mod high mid-plane neutral pressure is a consequence rather than a cause of confinement degradation. For high P_{mid}, heat convection and conduction by CX neutrals significantly enhance transport of heat from the core, as shown by Fig. 5.7.

It has been observed that the neutral gas bypass in the Alcator C-Mod divertor has a strong effect on T_e profiles measured across the SOL by the fast-scanning probe: the T_e profiles became steeper after the bypass was closed [6]. This can be a manifestation of the charge-exchange heat conduction in SOL. The bypass is geometrically close to the FSP, and closure of the bypass might have lowered the local density of neutrals, making the resulting cross-field heat diffusivity smaller.

In a recent numerical modeling of C-Mod edge plasma with the B2-EIRENE code it was also found that the SOL cross-field energy transport in C-Mod is dominated by convection rather than conduction [65]. However in the modeling in work [65] direct main chamber recycling was not properly included and the recycling coefficient in the divertor was artificially lowered which is unphysical according to the analysis in this chapter. Probably this is why in [65] a spatially dependent anomalous diffusion

coefficient was found sufficient to reproduce the SOL density profiles in C-Mod.

Similarly, in an earlier numerical modeling of C-Mod edge plasma with UEDGE spatially constant anomalous transport coefficients were found to give satisfactory match with the data [28]. And similarly, in work [28] main chamber recycling was not included and the recycling coefficient was artificially lowered.

However, in many edge modeling reports it was found, similarly to the present results, that a spatially-dependent $D_\perp$ (or a constant $D_\perp$ combined with a pinch) is needed to reproduce the SOL density profiles. In particular, in modeling of the ASDEX-Upgrade tokamak it was found that the anomalous diffusion coefficient in the SOL grows towards the wall [66]. The "shoulders" in the SOL density profiles found in C-Mod were also observed in ASDEX and ASDEX-Upgrade [66].

5.2.7 Conclusions

The present numerical modeling illustrates important features of the edge plasma in Alcator C-Mod. In the regime characterized by low P_{mid} ($\sim$ 0.01 mTorr) neutrals originating in the divertor chamber dominate the neutral population in the main chamber. However, in the regime characterized by high P_{mid} ($\sim$ 0.1-1 mTorr) recycling of plasma on the main chamber wall provides most of neutrals present in the main chamber. Draining of plasma by the poloidal flow is not significant for the main SOL where the particle balance is mostly radial.

The mid-plane gas pressure, P_{mid}, reflects the magnitude of particle transport from the core. In L-modes, P_{mid} grows rapidly (approximately cubically) with the core density, which indicates that the magnitude of plasma transport from the core grows rapidly with the core density.

In the high P_{mid} regime, heat convection due to the radial plasma flow and heat conduction by CX neutrals dominate the cross-field heat transport across the SOL, and

carry most of power across the LCFS. Even in the low P_{mid} regime heat conduction by CX neutrals dominates the cross-field heat transport in the outer regions of the SOL ($\rho \gtrsim 3mm$).

Chapter 6

Conclusions

This thesis has presented analysis and numerical modeling of transport in the edge plasma of the Alcator C-Mod tokamak. Several important results were obtained in the course of this work, providing a new understanding of some aspects of the physical picture of the edge plasma in C-Mod.

6.1 Summary

6.1.1 Anomalous heat diffusivity

Heat transport in the SOL was modeled by a steady-state 2-D heat conduction equation with classical parallel heat conduction and anomalous cross-field heat diffusivity. The anomalous cross-field heat diffusivity was then inferred by using experimental plasma temperature data as optimization constraints.

The anomalous $\chi_\perp$ were thus inferred for a few hundred of C-Mod discharges. It was found that the $\chi_\perp$ values are usually in the range 0.1-1 m^2/s. No significant correlation between $\chi_\perp$ and other parameters in the database was found. However it appeared that the subsets corresponding to open and closed bypass have quite

different $\chi_\perp$ values. For discharges with open bypass the inferred $\chi_{\perp 0}$ values are larger on average by a factor of about 3 than for those with bypass closed.
The effect of the neutral gas leak in the divertor on the inferred anomalous heat diffusivities can possibly be explained by effects of heat transport by CX neutral and/or heat convection.

6.1.2 Particle balance

Motivated by the finding of the effect of the bypass on the SOL temperature profiles an investigation of particle balance in the edge plasma in C-Mod was conducted. It resulted in a remarkable finding that, contrary to the traditional picture, in C-Mod plasma flux escaping from the core plasma primarily flows to the main chamber walls. Important implications of this finding include: (i) the particle diffusion coefficient grows across the SOL, (ii) the neutral pressure at the main chamber wall in C-Mod is set by anomalous particle transport across LCFS rather than by neutral baffling in the divertor, and (iii) heat convection is an important, maybe dominant, mechanism of energy transport across the LCFS.

6.1.3 Fluid modeling

To investigate further particle and energy transport in the edge plasma of Alcator C-Mod, a numerical modeling of C-Mod was conducted, using a multi-fluid code UEDGE which solves the plasma fluid equations in the real geometry. Confirming the previous conclusions this modeling illustrated important features of the edge plasma in Alcator C-Mod. The modeling showed that for typical values of P_{mid} ($\sim$ 0.1-1 mTorr) recycling of plasma on the main chamber wall provides most of neutrals present in the main chamber. The diffusion coefficient required to reproduce in the modeling the experimental SOL plasma density profiles had to be taken rapidly growing towards

the wall. Also it was found that usually heat convection due to the radial plasma flow and heat conduction by CX neutrals dominate the cross-field heat transport across the SOL, and carry most of power across the LCFS.

6.2 Discussion

The results presented in this thesis are in a clear disagreement with the traditionally accepted physical picture of the edge plasma in a divertor tokamak. In particular the picture of main chamber recycling dominating the particle balance for the main plasma contradicts the very concept of magnetic divertor which is supposed to deflect plasma particles towards a remote chamber.

As the C-Mod divertor does not perform one of its main functions to control the particle balance a question arises whether the situation can be changed by some "optimization" of the divertor geometry, possibly making its throat wider to accommodate more poloidal particle flux. This question is by no means well investigated. Still the author's opinion is that such modification would not improve the performance of the C-Mod divertor since: (i) the divertor throat is wide enough to accommodate 1-2 plasma density e-folding lengths, it is not clear how much wider it needs to be, (ii) making the divertor throat wider would degrade neutral gas baffling and thus would not allow for high "compression ratio" (P_{div}/P_{mid}), and (iii) with wider divertor it would be harder to achieve divertor detachment. As the physical size of a divertor is limited for a given tokamak, it may be that no divertor physically possible to build in C-Mod would be able to accomodate a poloidal flux competitive with the particle flux to the side wall.

Some recent reports from other tokamaks (AUG, JT60) also show that plasma interacts with the side wall more than it was usually thought, but in Alcator C-Mod this seems to be more explicit, which is apparently due to some specific features of

C-Mod (high density, high field, compact size). The role of plasma interaction with the side wall in other tokamaks deserves further analysis as it is critical for predicting the divertor performance in next generation tokamaks such as ITER.

6.3 Future work

The author would like to point out some important areas of future work in studying edge plasmas in C-Mod:

6.3.1 Kinetic modeling of neutral transport.

Many issues related to heat convection, heat conduction by CX neutrals, ionizations and recombination sources can be elucidated by modeling with neutral transport codes such as EIRENE or DEGAS. This would also provide important information for interpretation of experiments with the neutral gas bypass in C-Mod divertor.

6.3.2 Fluid modeling of drifts and currents.

Recent versions of edge codes such as UEDGE, B2.5 gained the capability to include fluid drifts and electric currents. Modeling of C-Mod with such advanced codes would be quite valuable for understanding of edge plasma asymmetries.

6.3.3 Experimental measurements of fluctuations.

Direct measurements of fluctuations in the edge plasma can help to understand the fundamental physics of edge transport. In particular one can measure directly the convective and conductive components of the anomalous heat flux. Studying correlations between fluctuations measured at different locations for the same field line can shed light on the problem of filamentary structure of edge turbulence.

6.3.4 Database analysis of anomalous transport coefficients.

The spectroscopy data along with neutral pressure measurements can be used to extract the anomalous diffusion coefficient, the heat diffusivity can probably be inferred after subtracting the convective component of the heat flux. Studying empirical trends in these coefficients using regression analysis and other methods may provide important information for theoretical understanding of the anomalous transport in the edge plasma.

Appendix A

General coordinates

In the tokamak the geometry is quite complicated which forces one to resort to the general coordinates. Here the author would like to give a brief overview of general coordinates as a reference. A more complete description of the general coordinates can be found elsewhere, for example see the book by D'haeseleer ([67]).

Consider a transformation by which the position vector $R(u^1, u^2, u^3)$ of any point in 3-D space is expressed as a function of three parameters u^1, u^2, u^3. Using components of R in a Cartesian system this transformation can be written as:

$$x = x(u^1, u^2, u^3), \;\; y = y(u^1, u^2, u^3), \;\; z = z(u^1, u^2, u^3) \tag{A.1}$$

If this transformation is non-singular it can be inverted:

$$u^1 = u^1(x, y, z), \;\; u^2 = u^2(x, y, z), \;\; u^3 = u^3(x, y, z) \tag{A.2}$$

This means that any point in 3-D space can be described by parameters u^1, u^2, u^3 thus they are coordinates as well. These general coordinates are called curvilinear coordinates.

Basis vectors

The tangent-basis vectors are defined by

$$e_1 = \frac{\partial R}{\partial u^1}, \quad e_2 = \frac{\partial R}{\partial u^2}, \quad e_3 = \frac{\partial R}{\partial u^3} \tag{A.3}$$

The tangent-basis vector e_i is tangent to the u^i-coordinate curve determined by fixing the other two coordinates. The tangent-basis vectors form local basis changing from point to point in the general case. One can define a unit tangent vector by normalizing it (no summation here)

$$\hat{e}_i = \frac{e_i}{|e_i|} \tag{A.4}$$

The magnitude $|e_i| = |\partial R/\partial u^i|$ is represented by symbol h_i and is called a metric coefficient or a scale factor.

Reciprocal basis vectors are defined by

$$e^i = \nabla u^i \tag{A.5}$$

Thus the reciprocal-basis vector e^i is orthogonal to the corresponding coordinate surface $u^i = const$. The relation between the tangent-basis vectors and the reciprocal-basis vectors is given by

$$e^i \cdot e_j = \delta^i_j \tag{A.6}$$

where δ^i_j is the Kroneker delta.

The two sets of basis vectors e^j and e_i form reciprocal sets of vectors. They can be expressed through each other by

$$e^i = \frac{e_j \times e_k}{e_i \cdot (e_j \times e_k)} \tag{A.7}$$

or conversely

$$e_i = \frac{e^j \times e^k}{e^i \cdot (e^j \times e^k)} \tag{A.8}$$

Covariant and contravariant components of a vector

A vector D can be writen as a linear combination of the vectors from either the tangent-basis vectors:

$$\vec{D} = (D \cdot e^1)e_1 + (D \cdot e^2)e_2 + (D \cdot e^3)e_3 = D^1 e_1 + D^2 e_2 + D^3 e_3 \tag{A.9}$$

or the reciprocal basis vectors:

$$\vec{D} = (D \cdot e_1)e^1 + (D \cdot e_2)e^2 + (D \cdot e_3)e^3 = D_1 e^1 + D_2 e^2 + D_3 e^3 \tag{A.10}$$

In the first case the coefficients D^i are called the **contravariant** components of vector D while in the second case the coefficients D_i are called the **covariant** components of vector D. There are no covariant and contravariant vectors as such in the three-dimensional physical space.

The physical component of a vector is the length of its orthogonal projection in a certain direction. This is what is actually measured physically. The physical components in the tangent-vector directions e_i denoted by $\tilde{A}_i$ are simply related to the contravariant components A^i:

$$\tilde{A}_i = A^i / h_i \tag{A.11}$$

Tensors

Tensors can be introduced via a dot-product between vectors. A dyad is **AB** is defined

by

$$X \cdot AB = (X \cdot A)B \tag{A.12}$$

or

$$AB \cdot X = A(B \cdot X) \tag{A.13}$$

where X is an arbitrary vector.

A dyad is a two-index object and can be written in the form

$$AB = A^i B^j e_i e_j \tag{A.14}$$

if both A and B are given in their contravariant components. A general second-order tensor $\mathbf{F}$ (also called a dyadic)

$$F = F^{ij} e_i e_j \tag{A.15}$$

cannot be written as an outer product of two vectors but it can be written as a sum of three dyads.

The metric coefficients g_{ij} are defined as the dot-product of the tangent-basis vectors:

$$g_{ij} = e_i \cdot e_j = \frac{\partial R}{\partial u^i} \cdot \frac{\partial R}{\partial u^j} \tag{A.16}$$

The metric coefficients g^{ij} are defined as the dot-product of the reciprocal-basis vectors:

$$g^{ij} = e^i \cdot e^j = \nabla u^i \cdot \nabla u^j \tag{A.17}$$

The scale factors h_i are related to the diagonal coefficient g_{ii}:

$$g_{ii} = h_i^2 \tag{A.18}$$

The differential arc length dl along a curve defined by infinitesimal increments of

coordiantes **du** is given by

$$(dl)^2 = g_{ij} du^i du^j \tag{A.19}$$

Once the metric coefficients g_{ij} and g^{ij} are known one can easily change contravariant vector components into covariant components and vice versa using relations:

$$D^i = g^{ij} D_j, \quad D_i = g_{ij} D^j \tag{A.20}$$

There is a relation between the metric coefficients g_{ij} and g^{ij}:

$$\delta_i^k = g^{kj} g_{ji} \tag{A.21}$$

and also

$$\delta_i^k = g_{ij} g^{jk} \tag{A.22}$$

In terms of matrix algebra this means that the product of matrices $[g_{ij}]$ and $[g^{ij}]$ is the identity matrix and thus these two matrices are inverse of each other. It follows for the determinants of these matrices that

$$g = det[g_{ij}] = 1/det[g^{ij}] \tag{A.23}$$

For coordinate transformation given by Eq. A.1 the Jacobian is by definition the determinant of the matrix formed by the nine partial derivatives

$$J \equiv \frac{\partial(x, y, z)}{\partial(u^1, u^2, u^3)} \tag{A.24}$$

The Jacobian **J** of the inverse transformation (Eq.A.2) is

$$\mathbf{J} = \frac{\partial(u^1, u^2, u^3)}{\partial(x, y, z)} \tag{A.25}$$

These two Jacobians are inverse of each other: $J = \mathbf{J}^{-1}$.

The determinant of the metric matrix $g = det[g_{ij}]$ is equal to the square of the Jacobian J: $g = J^2$. In a locally orthogonal coordinate system $J = \sqrt{g} = h_1 h_2 h_3$.

Vector operations in curvilinear coordinates

For two vectors A and B given in terms of their covariant or contravariant components

$$A = A^i e_i = A_i e^i \qquad (A.26)$$
$$B = B^i e_i = B_i e^i$$

the dot product in general curvilinear coordinates is

$$A \cdot B = g_{ij} A^i B^j = g^{ij} A_i B_j \qquad (A.27)$$

The magnitude of a vector is then

$$|A| = \sqrt{g_{ij} A^i A^j} = \sqrt{g^{ij} A_i A_j} \qquad (A.28)$$

The covariant components of the cross product of two vectors A and B in general coordinates are given by

$$(A \times B)_k = \epsilon_{ijk} \sqrt{g} A^i B^j \qquad (A.29)$$

and the contravariant components are given by

$$(A \times B)^k = \frac{\epsilon^{ijk}}{\sqrt{g}} A_i B_j \qquad (A.30)$$

where $\epsilon_{ijk} = \epsilon^{ijk}$ is the Levi-Civita tensor.

Differential operators

The ∇ operator can be introduced in the general coordinates by

$$\nabla = e^i \frac{\partial}{\partial u^i} \tag{A.31}$$

The gradient of a scalar function is given by

$$grad\Phi = \nabla\Phi = \frac{\partial \Phi}{\partial u^i} e^i \tag{A.32}$$

The divergence is given by

$$div\vec{A} = \nabla \cdot \vec{A} = \frac{1}{J}\frac{\partial (JA^i)}{\partial u^i} = \frac{1}{\sqrt{g}}\frac{\partial (\sqrt{g}A^i)}{\partial u^i} \tag{A.33}$$

The curl of a vector field is given by

$$\nabla \times A = \frac{\epsilon^{ijk}}{J}\frac{\partial A_j}{\partial u^i} e_k = \frac{\epsilon^{ijk}}{\sqrt{g}}\frac{\partial A_j}{\partial u^i} e_k \tag{A.34}$$

Transformation of vector and tensor components

Let two curvilinear coordinate systems be defined by transformations

$$u^j = u^j(x, y, z) \tag{A.35}$$

and

$$u^{j'} = u^{j'}(x, y, z) \tag{A.36}$$

Then there exists a direct transformation from u^j to $u^{j'}$ and vice versa:

$$u^{i'} = u^{i'}(u^i), \;\; u^i = u^i(u^{j'}) \tag{A.37}$$

All Jacobians are assumed to be non-zero.

The transformations of covariant vector components are

$$A_{i'} = A_j \frac{\partial u^j}{\partial u^{i'}}, \; A_j = A_{i'} \frac{\partial u^{i'}}{\partial u^j} \tag{A.38}$$

and for the contravariant components

$$A^{i'} = A^j \frac{\partial u^{i'}}{\partial u^j}, \; A^j = A^{i'} \frac{\partial u^j}{\partial u^{i'}} \tag{A.39}$$

Covariant components F_{ij} of a tensor transform like products of covariant vector components:

$$F_{i'j'} = F_{mn} \frac{\partial u^m}{\partial u^{i'}} \frac{\partial u^n}{\partial u^{j'}} \tag{A.40}$$

and

$$F_{ij} = F_{m'n'} \frac{\partial u^{m'}}{\partial u^i} \frac{\partial u^{n'}}{\partial u^j} \tag{A.41}$$

Contravariant components F_{ij} of a tensor transform like products of contravariant vector components:

$$F^{i'j'} = F^{mn} \frac{\partial u^{i'}}{\partial u^m} \frac{\partial u^{j'}}{\partial u^n} \tag{A.42}$$

and

$$F^{ij} = F^{m'n'} \frac{\partial u^i}{\partial u^{m'}} \frac{\partial u^j}{\partial u^{n'}} \tag{A.43}$$

Note that vectors and tensors are often introduced formally as objects whose components transform according to the above transformation rules Eq. (37-42).

Appendix B

Fluid equations

The behavior of ionized gas is described by the kinetic Boltzman equation for each species a (electrons e, ions i,neutrals n).

$$\frac{\partial f_a}{\partial t} + \frac{\partial}{\partial x_\beta}(v_\beta f_a) + \frac{\partial}{\partial v_\beta}(\frac{F_{a\beta}}{m_a} f_a) = C_a \tag{B.1}$$

For the case of charged particles the force $\vec{F}_a$ is

$$\vec{F}_a = e_a \vec{E} + e_a[vB] \tag{B.2}$$

where the E and B are smoothed macroscopic fields. The microfields arising for the particles at the close range are described by the collision term C_a. The collision term represents the effect of collisions of particles of species a with particles of other species

$$C_a = \Sigma_b C_{ab}(f_a, f_b) \tag{B.3}$$

Rather than describing plasma in detail by the means of the distribution function it can be sufficient to use certain average quantities: the number of particles per a unit

volume, n, the mean velocity of the particles. V, and the temperature.T.

$$n_a(t,r) = \int f_a(t,r,v)dv \tag{B.4}$$

$$V_a(t,r) = \frac{1}{n_a}\int v f_a(t,r,v)dv = < v >_a \tag{B.5}$$

$$T_a(t,r) = \frac{1}{n_a}\int \frac{m_a}{3}(v-V_a)^2 f_a(t,r,v)dv = \frac{m_a}{3} < (v-V_a)^2 > \tag{B.6}$$

Taking the first three moments of the kinetic equation one obtains the fluid transport equations:

-the equation for the density,

$$\frac{\partial n_a}{\partial t} + \nabla \cdot (n_a \vec{V}_a) = \int C_a d^3v \tag{B.7}$$

-the equation for the momentum density,

$$\frac{\partial}{\partial t}(n_a m_a \vec{V}_a) + \nabla \cdot (n_a m_a < \vec{v}\vec{v} >) - q_a n_a (\vec{E} + \vec{V}_a \times \vec{B}) = \int m_a \vec{v} C_a d^3v \tag{B.8}$$

-the equation for the kinetic energy density,

$$\frac{\partial}{\partial t}(n_a \frac{m_a < v^2 >}{2}) + \nabla \cdot (n_a \frac{m_a}{2} < \vec{v}v^2 >) - q_a n_a \vec{V}_a \cdot \vec{E} = \int \frac{m_a < v^2 >}{2} C_a d^3v \tag{B.9}$$

The velocity can be split into the average and deviation: $\vec{v} = \vec{V}_a + \vec{v}_r$, and the dyadic $< \vec{v}\vec{v} >$ in the momentum density equation splits into the ordered part and the random part:

$$< \vec{v}\vec{v} >= \vec{V}_a\vec{V}_a + < \vec{v}_r\vec{v}_r > \tag{B.10}$$

The latter defines the pressure tensor

$$\hat{P}_a = n_a m_a < \vec{v}_r \vec{v}_r >= n_a m_a \frac{v_r^2}{3}\hat{\delta} + \hat{\pi}_a = p_a \hat{\delta} + \hat{\pi}_a \tag{B.11}$$

where p_a is the scalar pressure and $\hat{\pi}_a$ is the viscous stress tensor which is the anisotropic part of the pressure tensor.

The right-hand side of the momentum equation is the momentum loss (friction force) due to collisions $\vec{R}_a$

$$\int m_a \vec{v} C_a d^3 v = \vec{R}_a \tag{B.12}$$

Using this notation the momentum equation can be written as

$$n_a m_a (\frac{\partial}{\partial t} + \vec{V}_a \cdot \nabla)\vec{V}_a + \nabla p_a = q_a n_a (\vec{E} + \vec{V}_a \times \vec{B}) + \vec{R}_a - \nabla \cdot \hat{\pi}_a \tag{B.13}$$

It can be also written in a sligtly different form:

$$\frac{\partial}{\partial t}(n_a m_a \vec{V}_a) + \nabla \cdot (n_a m_a \vec{V}_a \vec{V}_a) + \nabla \cdot \hat{\pi}_a = -\nabla p_a + q_a n_a (\vec{E} + \vec{V}_a \times \vec{B}) + \vec{R}_a \tag{B.14}$$

The viscous stress tensor becomes zero if the distribution function is spherically symmetric in the velocity space. Since the viscous stress tensor is a tensor of the second rank and depends on the partial derivatives $\partial V_{a,i}/\partial x_j$ it is conventionally written in the form

$$\hat{\pi} = -\eta(\frac{\partial V_i}{\partial x_j} + \frac{\partial V_j}{\partial x_i} - \frac{2}{3}\delta_{ij}\frac{\partial V_k}{\partial x_k}) - \zeta \delta_{ij}\frac{\partial V_k}{\partial x_k} \tag{B.15}$$

where parameters η and ζ are the coefficients of the shear and bulk viscosity.

For the case of η and ζ constant one can write

$$\nabla \cdot \hat{\pi} = -\eta \nabla^2 \vec{V} - (\frac{\eta}{3} + \zeta)\nabla(\nabla \cdot \vec{V}) \tag{B.16}$$

Then the momentum equation can be written in the Navier-Stokes form:

$$n_a m_a (\frac{\partial}{\partial t} + \vec{V}_a \cdot \nabla)\vec{V}_a = -\nabla p_a + \eta \nabla^2 \vec{V}_a + (\frac{\eta}{3} + \zeta)\nabla(\nabla \cdot \vec{V}_a) + q_a n_a (\vec{E} + \vec{V}_a \times \vec{B}) + \vec{R}_a \tag{B.17}$$

In the left-hand side of the energy equation the energy density can be split into the ordered and random parts

$$n_a \frac{m_a < v^2 >}{2} = n_a \frac{m_a V_a^2}{2} + n_a \frac{m_a < v_r^2 >}{2} = n_a \frac{m_a V_a^2}{2} + \frac{3}{2} p_a \tag{B.18}$$

Next, separating the ordered and the random parts in the energy flux one finds

$$n_a \frac{m_a}{2} < \vec{v} v^2 > = n_a \frac{m_a}{2} \vec{V}_a V_a^2 + n_a \frac{m_a}{2} < v_r^2 > \vec{V}_a + n_a \frac{m_a}{2} < \vec{v}_r v_r^2 > + n_a \frac{m_a}{2} \vec{V}_a \cdot < \vec{v}_r \vec{v}_r > \tag{B.19}$$

where on the right-hand side the first term is the ordered flow of ordered kinetic energy, the second term is heat convection, the third term is the conducted heat, $\vec{q}$, the last term is the rate of work done by the pressure forces.

The collisional term in the energy equation becomes

$$\int \frac{m_a < v^2 >}{2} C_a d^3 v = \int \frac{m_a < v_r^2 >}{2} C_a d^3 v + \vec{V}_a \cdot \int m_a \vec{v}_r C_a d^3 v = Q_a + \vec{V}_a \cdot \vec{R}_a \tag{B.20}$$

where Q_a is the heat generated in collisions.

Now the the kinetic energy density equation can be written as

$$\frac{\partial}{\partial t}(n_a\frac{m_aV_a^2}{2}+\frac{3}{2}p_a)+\nabla\cdot[(n_a\frac{m_aV_a^2}{2}+\frac{5}{2}p_a)\vec{V}_a+\vec{V}_a\cdot\hat{\pi}_a+\vec{q}_a]=q_an_a\vec{V}_a\cdot\vec{E}+\vec{V}_a\cdot\vec{R}_a+Q_a \tag{B.21}$$

The momentum equation dot multiplied by $\vec{V}_a$ gives the ordered kinetic energy density equation:

$$\frac{\partial}{\partial t}(n_a\frac{m_aV_a^2}{2})+\nabla\cdot(n_a\frac{m_aV_a^2}{2}\vec{V}_a)=q_an_a\vec{V}_a\cdot\vec{E}+\vec{V}_a\cdot\vec{R}_a-\vec{V}_a\cdot(\nabla\cdot\hat{P}_a) \tag{B.22}$$

Subtracting it from the energy equation gives the internal energy density equation

$$\frac{\partial}{\partial t}(\frac{3}{2}n_aT_a)+\nabla\cdot(\frac{5}{2}p_a\vec{V}_a+\vec{q}_a)=\vec{V}_a\cdot\nabla p_a-\hat{\pi}_a:\nabla\vec{V}_a+Q_a \tag{B.23}$$

Bibliography

[1] David L. Book. NRL Plasma Formulary. Naval Research Laboratory, Washington, DC 20375, 1990.

[2] John Wesson. *Tokamaks.* Clarendon Press, Oxford, 1997.

[3] L. Spitzer. Technical Report NYO-993, U.S. Atomic Energy Comission, 1951.

[4] R. Chodura. Plasma flow in the sheath and presheath of a scrape-off layer. In *Physics of Plasma-Wall Interactions in Controlled Fusion*, pages 99–134, New York and London, 1986. Plenum Press.

[5] P. J. Harbour et al. *J. Nucl. Mater.*, 128-129:359, 1984.

[6] B. LaBombard et al. Experimental investigation of transport phenomena in the scrape-off layer and divertor of Alcator C-Mod. *J. Nucl. Mater.*, 241-243:149, 1997.

[7] J. A. Boedo et al. Measurements of flows in the DIII-D divertor by Mach probes. *J. Nucl. Mater.*, 266-269:783, 1999.

[8] P. C. Stangeby and G. McCracken. Plasma boundary phenomena in tokamaks. *Nucl. Fusion*, 30(7):1225, 1990.

[9] P. C. Liewer et al. Temperature fluctuations and heat transport in the edge regions of a tokamak. *Phys. Fluids*, 29:309, 1986.

[10] C. Ritz et al. Fluctuation-induced energy flux in the tokamak edge. *Phys. Rev. Lett.*, 62:1844, 1989.

[11] G. Fiksel et al. Magnetic fluctuation-induced heat transport. *Plasma Phys. Control. Fusion*, 38:A213, 1996.

[12] B. Scott. Three-dimensional computation of drift Alfven turbulence. *Plasma Phys. Control. Fusion*, 39:1635–1668, 1997.

[13] M. Endler. Turbulent SOL transport in stellarators and tokamkas. *J. Nucl. Mater.*, 266-269:84–90, 1999.

[14] W. L. Rowan et al. TEXT particle confinement. *Nucl. Fusion*, 27:1105, 1987.

[15] J. W. Connor et al. Comparision of theoretical models for scrape-off layer widths with data from COMPASS-D, JET and Alcator C-Mod. Technical Report UKAEA FUS 396, UKAEA/Euratom Fusion Association, 1998.

[16] X. Garbet et al. A model for the turbulence in the scrape-off layer of tokamaks. *Nucl. Fusion*, 31:967, 1991.

[17] A. Zeiler, J. F. Drake, and D. Biskamp. A model for the turbulence in the scrape-off layer of tokamaks. *Phys. Plasmas*, 4:991, 1997.

[18] A. L. M. Rogister and Ding Li. *Nucl. Fusion*, 33:1799, 1993.

[19] D. R. McCarthy et al. Non-linear behavior of radiative modes in non-coronal equilibrium. *Phys. Plasmas*, 4:2567, 1997.

[20] X. Q. Xu and R. H. Cohen. Scrape-off layer turbulence theory and simulations. *Contributions to Plasma Physics*, 38:158–170, 1998.

[21] N. Asakura et al. *J. Nucl. Mater.*, 241-243:559, 1997.

[22] M.V.Umansky and B.LaBombard. Empirical scalings of cross-field diffusivities in the scrape-off layer of Alcator C-Mod from a 2-D interpretive model. *J. Nucl. Mater.*, 266-269:721–725, 1999.

[23] K. McCormick et al. ITER edge database investigations of the SOL width. *J. Nucl. Mater.*, 266-269:99–108, 1999.

[24] G. Counsell et al. SOL width scaling from consideration of edge transport in tokamaks. *J. Nucl. Mater.*, 266-269:91–98, 1999.

[25] C. S. Pitcher and P. C. Stangeby. Experimental divertor physics. *Plasma Phys. Control. Fusion*, 39:779, 1997.

[26] P. C. Stangeby. The plasma sheath. In *Physics of Plasma-Wall Interactions in Controlled Fusion*, pages 931–1004, New York and London, 1986. Plenum Press.

[27] M. E. Fenstermacher et al. UEDGE and DEGAS modeling of the DIII-D scrape-off layer plasma. *J. Nucl. Mater.*, 220-222:330–335, 1995.

[28] F. Wising et al. Simulation of the Alcator C-Mod divertor with an improved neutral fluid model. *Contributions to Plasma Physics*, 36(2/3):136, 1996.

[29] W.H. Press, S.T. Teukolsky, W.T. Vetterling, and B.P. Flannery. *Numerical Recipes in C.* Cambridge University Press, 1991.

[30] A. N. Tikhonov. *Mathematical models and numerical methods.* "PWN–Polish Scientific Publishers", Warszawa, 1978.

[31] IMSL: Fortran subroutines for mathematical applications. IMSL, Inc., 1991.

[32] A. N. Tikhonov. *Partial differential equations of mathematical physics.* Holden-Day, San Francisco, 1964.

[33] L.L. Lao, H.St. John, R.D. Stambaugh, A.G. Kellman, and W. Pfeiffer. Reconstruction of current profile parameters and plasma shapes in tokamaks. *Nucl. Fusion*, 25(11), 1985.

[34] B. Flury and H. Riedwyl. *Multivariate statistics: a practical approach.* Chapman and Hall, London, 1988.

[35] B.R. Martin. *Statistics for physicists.* Academic Press, London, 1971.

[36] I. H. Hutchinson. *Introduction to plasma diagnostics.* Cambridge University Press, 1987.

[37] A.Niemczewski. *Neutral particle dynamics in the Alcator C-Mod tokamak.* PhD thesis, Massachusetts Institute of Technology, Department of Nuclear Engineering, 1995.

[38] C. S. Pitcher et al. Divertor bypass experiments in Alcator C-Mod. In *26th EPS conference on controlled fusion and plasma physics*, Maastricht, the Netherlands, 1999.

[39] B. LaBombard. Private communication, 1999.

[40] F.Wagner and K.Lackner. Divertor tokamak experiments. In *Physics of Plasma-Wall Interactions in Controlled Fusion*, pages 931–1004, New York and London, 1986. Plenum Press.

[41] I.H.Hutchinson et al. First results from Alcator C-Mod. *Phys. Plasmas*, 1:1511, 1994.

[42] M. V. Umansky, S. I. Krasheninnikov, B. LaBombard, and J. L. Terry. Comments on particle and energy balance in the edge plasma of Alcator C-Mod. *Phys. Plasmas*, 5:3373, 1998.

[43] L.C.Johnson and E.Hinnov. Ionization, recombination and radiation in hydrogen plasma. *J.Quant.Spectrosc.Radiat.Transfer*, 13:333, 1973.

[44] B. Lipschultz et al. Ultrahigh densities and volume recombination inside the separatrix of the Alcator C-Mod tokamak. *Phys. Rev. Lett.*, 81:1007, 1998.

[45] T.Fujimoto, S.Miyachi, and K.Sawada. New density diagnostic method based on emission line intensity ratio of neutral hydrogen in an ionizing phase plasma. *Nucl. Fusion*, 28:1255, 1988.

[46] C.Kurz. *Tomography of light emission from the plasma edge of Alcator C-Mod.* PhD thesis, Massachusetts Institute of Technology, Department of Nuclear Engineering, 1995.

[47] J. Terry. Private communication, 1999.

[48] R. Schneider et al. Role of divertor geometry on detachment in ASDEX Upgrade. *J. Nucl. Mater.*, 266-269:175, 1999.

[49] H.-S. Bosch et al. Noble gas exhaust with a strongly baffled divertor in ASDEX Upgrade. *J. Nucl. Mater.*, 266-269:462, 1999.

[50] J. Schweinzer et al. Comparison of scrape-off layer behavior between DIV-I and DIV-II operations in ASDEX Upgrade. *J. Nucl. Mater.*, 266-269:934, 1999.

[51] R. Schneider et al. Divertor geometry optimization for ASDEX Upgrade. *J. Nucl. Mater.*, 241-243:701, 1997.

[52] G. Porter. The role of radial particle flow on particle balance in DIII-D. *Phys. Plasmas*, 5:4311, 1998.

[53] R. D. Monk. Recent results from divertor and SOL studies at JET. Submitted to the Nuclear Fusion.

[54] N. Asakura et al. Heat and particle transport of SOL/divertor plasma in the W-shaped divertor on JT-60U. In *17th IAEA Fusion Energy Conference*, 1998.

[55] M. V. Umansky, S. I. Krasheninnikov, B. Lipschultz, B. LaBombard, and J. L. Terry. Modeling of particle and energy transport in the edge plasma of Alcator C-Mod. *Phys. Plasmas*, 6:2793, 1999.

[56] S.I. Braginskii. Transport processes in a plasma. *Reviews of Plasma Physics*, 1:205, 1965.

[57] T. D. Rognlien, J. L. Milovich, M. E. Rensink, and G. D. Porter. A fully implicit, time dependent 2-D fluid code for modeling tokamak edge plasmas. *J. Nucl. Mater.*, 196-198:347–351, 1992.

[58] T. D. Rognlien. Private communication, 1997.

[59] An introduction to the 2-D fluid code UEDGE. In file uedge.man in UEDGE distribution.

[60] I. H. Hutchinson et al. The effect of field reversal on the Alcator C-Mod divertor. *Plasma Phys. Control. Fusion*, 37:1389, 1995.

[61] M. Greenwald et al. Transport experiments in Alcator C-Mod. *Phys. Plasmas*, 2:2308, 1995.

[62] S. Kaye et al. Attainment of high confinement in neutral beam heated divertor discharges in the PDX tokamak. *J. Nucl. Mater.*, 121:115, 1984.

[63] K. McCormick et al. Effects of edge conditions on plasma confinement in ASDEX. *J. Nucl. Mater.*, 176-177:89, 1990.

[64] L. D. Horton et al. High density divertor operations in JET. *Plasma Phys. Control. Fusion*, 38(12A), 1996.

[65] A. Loarte et al. Comparison of B2-EIRENE calculations with multi-machine experimental measurements. *J. Nucl. Mater.*, 266-269:1123, 1999.

[66] H.-S. Bosch et al. 2D modeling of the ASDEX-Upgrade scrape-off layer and divertor plasma. *J. Nucl. Mater.*, 220-222:558–562, 1995.

[67] W. D. D'haeseleer, W. N. G. Hichton, J. D. Callen, and J. L. Shohet. *Flux coordinates and magnetic field structure.* Springer-Verlag, New York, 1991.